Critical assessment of efficient numerical methods for a long-term simulation of heat and moisture transfer in porous materials

Madina Abdykarim, Julien Berger, Denys Dutykh, Lucile Soudani, Amen Agbossou

HAL Id: hal-02162803
https://hal.science/hal-02162803v2

Submitted on 3 Sep 2019

Critical assessment of efficient numerical methods for a long-term simulation of heat and moisture transfer in porous materials

Madina Abdykarim[a*], Julien Berger[a], Denys Dutykh[b],
Lucile Soudani[c], Amen Agbossou[a]

September 4, 2019

[a] Univ. Grenoble Alpes, Univ. Savoie Mont Blanc, UMR 5271 CNRS, LOCIE, 73000 Chambéry, France
[b] Univ. Grenoble Alpes, Univ. Savoie Mont Blanc, UMR 5127 CNRS, LAMA, 73000 Chambéry, France
[c] LGCB-LTDS, UMR 5513 CNRS, ENTPE, Univ. de Lyon, 69100 Vaulx-en-Velin, France
*Corresponding author, e-mail address : Madina.Abdykarim@univ-smb.fr

Abstract

The issue to predict the behavior of building materials during wide horizons of time is still challenging. Experimental set-ups, since they require to perform tests for several years, are costly, never at the full scale and inconvenient. Building Performance Simulation (BPS) programs are designed to perform predictions on computational machines and cut experimental costs significantly. Nonetheless, in the recent review of state–of–the–art, it was indicated that despite the wide range of programs, there are still some drawbacks in terms of the accuracy and the high computational cost. This paper investigates the application of an innovative numerical method, called Super–Time–Stepping (STS) method. It allows performing accurate simulations with time-steps much larger than with standard explicit approaches. These "super" time-steps also enable us to reduce the computational cost. In addition to that, the design of the method allows easier application for models in higher dimensions and with nonlinear parameters. The efficiency of the method is tested on linear and nonlinear academic cases. Further study for the reliability of the model is performed on an experimental case study. The experiment has been carried out on a rammed earth wall during almost 14 months. Obtained data is presented in this article and implemented into proposed model. As a result of the case studies, it is shown that in comparison to the EULER explicit method, the STS methods can cut costs by more than five times while maintaining high accuracy and efficiency. A very fine analysis of the physical phenomena is also performed.

Keywords: porous material; numerical simulation; heat and moisture transfer; super–time–stepping; rammed earth; long-term simulation

Contents

1 Introduction

Assessing the long-term behavior of building envelope's moisture damage is crucial [1, 2]. Experimental set-ups are costly, never at the full scale and inconvenient since they require to perform tests for several years. Various Building Performance Simulation (BPS) programs are established to perform predictions on computational machines and cut experimental costs significantly. To list only a few, one can mention DELPHIN [3], WUFI [4] and Domus [5]. These programs include numerical models to simulate, among other phenomena, coupled heat and moisture transfer.

The physical phenomena of coupled heat and moisture transfer have been studied in depth from the 1950s [6]. Since then, there is no consensus on the numerical strategies to solve such class of nonlinear parabolic problems [7–15]. On one hand, the traditional explicit methods are simple and accurate to implement. It can also be argued, that the best practice to solve coupled problems numerically is to employ the explicit numerical schemes. However, problems with a nonlinear behavior of the materials necessitates very fine space and time discretizations (especially for a long-term or a whole building scale simulations). As a result, classical explicit approaches are overly restrictive for the choice of time-steps to satisfy the numerical stability. On the other hand, there are implicit schemes, which are free from stability conditions and moderately efficient but can be comparatively complicated to use in practice. They lack robustness for sufficiently nonlinear problems by requiring sub-iterations to treat nonlinearities. This, in turn, considerably increases computational costs. In the works of CLARK and KAVETSKI [16, 17] the traditional time-stepping methods have been critically evaluated by their fidelity and efficiency. It was shown that each of the classical methods has certain restrictions. Need for innovative approaches has been highlighted. The goal of this article is to demonstrate that there exists a class of robust methods.

Among others, two main limitations of traditional methods implemented in BPS programs are discussed in this article. They are the high computational cost and the choice of a very fine numerical grid. The innovative numerical schemes proposed in this work enable to overcome both of them while retaining the advantages of an explicit formulation.

Despite its history of almost 40 years [18], the group of methods called Super–Time–Stepping (STS) is novel to the state-of-the-art of building simulations. It has already proved to be sufficiently efficient in decent studies from applied mathematics [19–22]. But it is employed only for a limited range of parabolic problems and almost never practically used. This is unfortunate, because, first of all, the method claims to be a very powerful tool to cut computational costs in a very simple way. Basically, it enables to relax stability restriction for a time discretization of the explicit scheme by performing a certain number of "jumps" over several time-steps. If the number of these jumps is N_{S}, then the new time-step shall be at least N_{S}^{2} times bigger than the explicit one. As the stability is forced only on big steps (or supersteps), the computational gain is proportional to the number of supersteps, N_{S}. The advantages can be quite dramatic as N_{S} increases.

Secondly, compared to the unconditionally stable implicit schemes, the STS method is much easier to implement (thanks to an explicit formulation). The design of the method implies easier applications for models in higher dimensions and with nonlinear properties. The notable applications to linear and nonlinear parabolic problems were performed in [23–25]. In the works of ALEXIADES [24, 25], the method was inspired by the recursion relations associated with the CHEBYSHEV polynomials. The STS method was then further developed by MEYER *et al.* [20, 21] by introducing the methods based on the recursion relations of the shifted LEGENDRE polynomials. The properties of both polynomials allow ensuring the stability of the method at the end of

each iteration stage, *i.e.* at the end of a cycle of N_{S} time-steps. Consequently, it is believed that with the STS method it possible to employ the discretization with larger super-time-steps and to cut computational costs.

In this work, it shall be proved that the STS method can be far more efficient than the well-known EULER explicit scheme in application to the building heat and mass transfer phenomena. Another improved explicit approach, namely DU FORT–FRANKEL method is used for a critical assessment of the STS method. The method was deeper explored in the works of GASPARIN *et al.* [26, 27].

As the first evaluation step, the schemes will be validated for two case studies of linear and nonlinear heat and moisture transfer models. The application to the real case study will be the next step to validate the fidelity of the proposed numerical models for long-term simulations. Then, the predictions of the numerical models shall be compared with more than 14 months of experimental observations, obtained in previous investigations for the drying of a rammed earth wall [28–30].

The article is organized as follows. The mathematical model to reproduce the physical phenomena is presented in Section 2. It follows with the description of the numerical methods in Section 3. Validation of the reliability and accuracy of schemes are performed for two cases with linear and nonlinear material properties in Section 4. Finally, after successful tests, the proposed methods are assessed for their fidelity by application to a real case study. A broad presentation of the experimental set-up, the physical phenomena and the numerical application are detailed in Section 5.

2   Mathematical Model

This section provides a short summary of the general formulation of the heat and moisture transfer phenomena. Governing equations are synthesized from expressions of physical flows. Boundary conditions are written as a linear combination of temperature and moisture concentration differences. The adopted procedure to calculate the vapor concentration difference is also presented. In the end, the dimensionless formulation is described for the governing equations and the boundary conditions.

2.1   Heat and mass balance

The governing equations are based on the conservation equation for liquid and vapor masses, and on the energy conservation equation [31–33]. The model is formulated for the one-dimensional heat and moisture transfer through a porous material. The equations are defined by the spatial domain $\Omega_x = [0, \ell]$ and the time domain $\Omega_t = [0, \tau]$, where $\ell \, [\, \mathsf{m} \,]$ is the thickness of a wall and $\tau \, [\, \mathsf{h} \,]$ is the final time. The material is represented by a solid matrix and fulfilled in the pores by water in vapor and liquid states. The dry air phase is not taken into account in the model. The schematic representation of the wall is illustrated in Figure 1. The subscripts 0, 1 and 2 represent the dry state of the material, the water vapor and the liquid water, respectively. The mass balance reads as in [32]:

$$\rho_2 \cdot \frac{\partial \theta}{\partial t} = -\frac{\partial j_{12}}{\partial x}, \tag{2.1}$$

where $\rho_2 \, [\, \mathsf{kg/m^3} \,]$ is the specific mass of liquid water and $\theta \, [\, \varnothing \,]$ is the volumetric moisture (liquid plus vapor) content. Density of the moisture flow rate, $j_{12} \, [\, \mathsf{kg/(m^2 \cdot s)} \,]$, includes the water vapor flow rate j_1 and the liquid water flow rate j_2, so that $j_{12} \equiv j_1 + j_2$.
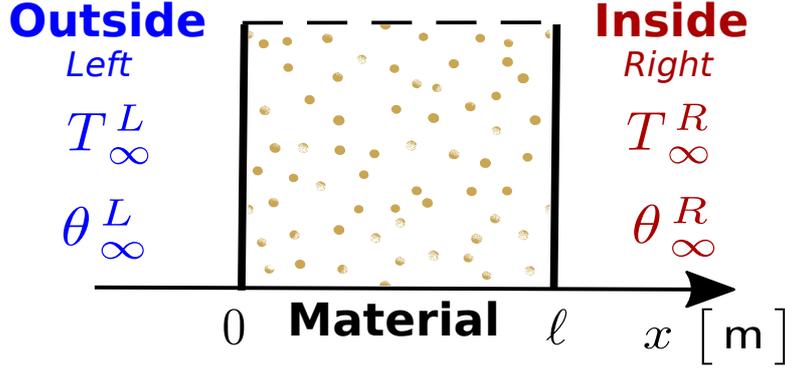
4

Figure 1: The schematic representation of the wall.

The energy conservation equation enables to compute the temperature $T \left[\mathsf{K} \right]$ evolution as in [32]:

$$\left(\rho_0 \cdot c_0 \,+\, \rho_2 \cdot c_2 \cdot \theta \right) \cdot \frac{\partial T}{\partial t} \;=\; -\,\frac{\partial j_{\mathsf{q}}}{\partial x} \,-\, L_{12}^{\circ} \cdot \frac{\partial j_1}{\partial x} \,, \tag{2.2}$$

where $\rho_0 \left[\mathsf{kg/m^3} \right]$ is the specific mass of the dry material, $c_0 \left[\mathsf{J/(kg \cdot K)} \right]$ is the material heat capacity and $c_2 \left[\mathsf{J/(kg \cdot K)} \right]$ is the water heat capacity. The quantity $j_{\mathsf{q}} \left[\mathsf{W/m^2} \right]$ is a sensible heat flow rate. The latent heat of vaporization $L_{12}^{\circ} \left[\mathsf{J/kg} \right]$ is taken as a positive constant value.

2.2   Expression of the flows

The total moisture flow rate can be expressed depending on the temperature $T \left[\mathsf{K} \right]$ and moisture $\theta \left[\varnothing \right]$ gradients ([31, 32]):

$$j_{12} \;=\; -\left(D_\theta \cdot \frac{\partial \theta}{\partial x} \,+\, D_T \cdot \frac{\partial T}{\partial x} \right), \tag{2.3}$$

where $D_\theta \left[\mathsf{m^2/s} \right]$ is the diffusion coefficient under moisture gradient and $D_T \left[\mathsf{m^2/(s \cdot K)} \right]$ is the diffusion coefficient under temperature gradient. D_θ and D_T are functions of T and θ:

$$D_\theta \,:\, (T, \theta) \,\mapsto\, D_\theta (T, \theta) \,,$$
$$D_T \,:\, (T, \theta) \,\mapsto\, D_T (T, \theta) \,.$$

The sensible heat flow rate j_{q} is defined using the FOURIER law:

$$j_{\mathsf{q}} \;=\; -\,k_T \cdot \frac{\partial T}{\partial x} \,, \tag{2.4}$$

where $k_T \left[\mathsf{W/(m \cdot K)} \right]$ is the thermal conductivity of the material, that depends on T and θ:

$$k_T \,:\, (T, \theta) \,\mapsto\, k_T (T, \theta) \,.$$

Lastly, the vapor flow rate j_1 is written as in [31, 32, 34]:

$$j_1 \;=\; -\,k_{TM} \cdot \frac{\partial \theta}{\partial x} \,, \tag{2.5}$$

where $k_{TM} \left[\mathsf{kg/(m \cdot s)} \right]$ is the vapor transfer coefficient under a moisture gradient, defined as follows:

$$k_{TM} \,:\, (T, \theta) \,\mapsto\, k_{TM} (T, \theta) \,.$$

It should be noted that the vapor transfer coefficient under the temperature gradient (the so-called SORET effect) can be neglected in building components [34, 35].

5

2.3 Governing equations

For the sake of clarity, the so-called global heat storage coefficient $c_T \left[\mathsf{W} \cdot \mathsf{s}/(\mathsf{m}^3 \cdot \mathsf{K}) \right]$ is introduced as in [36]:

$$c_T \, : \, \theta \mapsto \rho_0 \cdot c_0 \, + \, \rho_2 \cdot c_2 \cdot \theta \, .$$

Using the expression of the flow rate given by Equations (2.3) – (2.5) combined with the mass and heat balance Equations (2.1) and (2.2) respectively, the mathematical model can be expressed as:

$$\rho_2 \cdot \frac{\partial \theta}{\partial t} \; = \; \frac{\partial}{\partial x} \left(D_\theta \cdot \frac{\partial \theta}{\partial x} \, + \, D_T \cdot \frac{\partial T}{\partial x} \right) , \tag{2.6a}$$

$$c_T \cdot \frac{\partial T}{\partial t} \; = \; \frac{\partial}{\partial x} \left(k_T \cdot \frac{\partial T}{\partial x} \right) \, + \, L_{12}^{\circ} \cdot \frac{\partial}{\partial x} \left(k_{TM} \cdot \frac{\partial \theta}{\partial x} \right) , \tag{2.6b}$$

which is a system of two coupled partial differential equations with respect to two unknowns T and θ.

2.4 Boundary conditions

At the interface between the material and the ambient air, the sensible heat flow rate j_q depends on the values at the interface and the ambient air conditions:

$$\mathbf{n} \cdot (j_q) \; = \; h_T \cdot \left(T \, - \, T_\infty \right) , \tag{2.7}$$

where $\mathbf{n} \in \{ -1 \, , \, 1 \}$ is the outward unit normal vector, projected on the O_x axis. The vector assumes $+1$ at the left and -1 at the right boundary sides (see Figure 1 for the schematic representation of the wall). $h_T \left[\mathsf{W}/(\mathsf{m}^2 \cdot \mathsf{K}) \right]$ is the surface heat transfer coefficient, which is also a function of time t:

$$h_T \, : \, t \mapsto h_T \left(t \right) ,$$

T is the surface temperature at $x \; = \; \{ 0 , \ell \}$, T_∞ is the ambient air temperature given as a function of time $t \in [0 , \tau]$:

$$T_\infty \, : \, t \mapsto T_\infty \left(t \right) .$$

According to MENDES *et al.* [32], the assumption is made that moisture flow between a porous medium and the air can be written as a function of a vapor concentration difference:

$$\mathbf{n} \cdot (j_1) \; = \; h_M \cdot \left(\rho_1 \, - \, \rho_{1,\infty} \right) , \tag{2.8}$$

with $\rho_1 \left[\mathsf{kg}/\mathsf{m}^3 \right]$ being the vapor concentration at the surface $(x \; = \; \{ 0 , \ell \})$. $\rho_{1,\infty}$ is the vapor concentration in the ambient air, which is taken as the time dependent variable:

$$\rho_{1,\infty} \, : \, t \mapsto \rho_{1,\infty} \left(t \right) ,$$

The parameter $h_M \left[\mathsf{m}/\mathsf{s} \right]$ is the surface vapor transfer coefficient, defined as a function of time t:

$$h_M \, : \, t \mapsto h_M \left(t \right) ,$$

It is possible to present the vapor concentration difference as a combination of the temperature and moisture concentration differences. For this purpose, the first step is to assume, that the water

vapor behaves as a perfect gas. Also, one can recall that the vapor pressure can be written as a product of the saturated pressure $P_{\text{sat}}\,\big[\,\mathsf{Pa}\,\big]$ and the relative humidity $\varphi\,\big[\,\varnothing\,\big]$, which yields:

$$\rho_1 \;-\; \rho_{1,\infty} \;=\; \frac{P_{\text{sat}} \cdot \varphi \cdot M}{R_1 \cdot T} \;-\; \frac{P_{\text{sat},\infty} \cdot \varphi_\infty \cdot M}{R_1 \cdot T_\infty}$$

or,

$$\rho_1 \;-\; \rho_{1,\infty} \;=\; \frac{\varphi_\infty \cdot M}{R_1} \cdot \left(\frac{P_{\text{sat}}}{T} \;-\; \frac{P_{\text{sat},\infty}}{T_\infty} \right) \tag{2.9}$$
$$+\; \frac{M}{R_1} \cdot \frac{P_{\text{sat}}}{T} \cdot \Big(\varphi \;-\; \varphi_\infty \Big),$$

where $R_1\,\big[\,\mathsf{J}/(\,\mathsf{kg}\cdot\mathsf{K}\,)\,\big]$ is the gas constant of vapor, $M\,\big[\,\mathsf{kg/mol}\,\big]$ is the molecular mass, P_{sat}, $P_{\text{sat},\infty}$ and φ, φ_∞ stand for the saturated pressure and the relative humidity on the surface and of the air respectively. The saturation pressure P_{sat} is a function of temperature T and can be approximated according to [37] as follows:

$$P_{\text{sat}} \;:\; T \;\mapsto\; \exp\left(65.81 \;-\; \frac{7066.27}{T} \;-\; 5.97 \cdot \log\left(T \right) \right).$$

It is also important to note that the relative humidity φ depends on the moisture content θ of the material:

$$\varphi \;:\; \theta \;\mapsto\; \varphi\left(\theta \right).$$

The relative humidity can also be calculated as a first-degree function with small errors for a certain range of the moisture content. According to MENDES *et al.* [32], by introducing a residual function r related to the moisture content on the surface, one can increase accuracy of such substitutions. Therefore, one can write the following functions:

$$r \;:\; \theta \;\mapsto\; \varphi\left(\theta \right) \;-\; \widetilde{\varphi}\left(\theta \right),$$

where $\widetilde{\varphi} \;:\; \theta \;\mapsto\; A \cdot \theta$, with A being a coefficient from linear approximation of function $\varphi\left(\theta \right)$ (see Figure 2). Using the first order TAYLOR expansion [38], the function $\widetilde{\varphi}\left(\theta \right)$ can be written in the other way as:

$$\widetilde{\varphi}\left(\theta \right) \;=\; \varphi\left(\theta_\infty \right) \;+\; \frac{d\widetilde{\varphi}}{d\theta} \cdot \Big(\theta \;-\; \theta_\infty \Big) \;+\; \mathcal{O}\Big(\left(\theta \;-\; \theta_\infty \right)^2 \Big), \qquad \text{as } \theta \to \theta_\infty,$$

where θ is the surface moisture content at $x \;=\; \{\,0,\,L\,\}$. The moisture content in the ambient air θ_∞ is taken as a time dependent variable:

$$\theta_\infty \;:\; t \;\mapsto\; \theta_\infty\left(t \right).$$

Thereby, the second term on the right-hand-side of Equation (2.9) becomes:

$$\varphi \;-\; \varphi_\infty \;=\; \frac{d\widetilde{\varphi}}{d\theta} \cdot \Big(\theta \;-\; \theta_\infty \Big) \;+\; r\left(\theta \right).$$

Finally, Equation (2.9) is written as:

$$\rho_1 \;-\; \rho_{1,\infty} \;=\; \frac{\varphi_\infty \cdot M}{R_1} \cdot \left(\frac{P_{\text{sat}}}{T} \;-\; \frac{P_{\text{sat},\infty}}{T_\infty} \right)$$
$$+\; \frac{M}{R_1} \cdot \frac{P_{\text{sat}}}{T} \cdot \left(\frac{d\widetilde{\varphi}}{d\theta} \cdot \Big(\theta \;-\; \theta_\infty \Big) \;+\; r\left(\theta \right) \right).$$
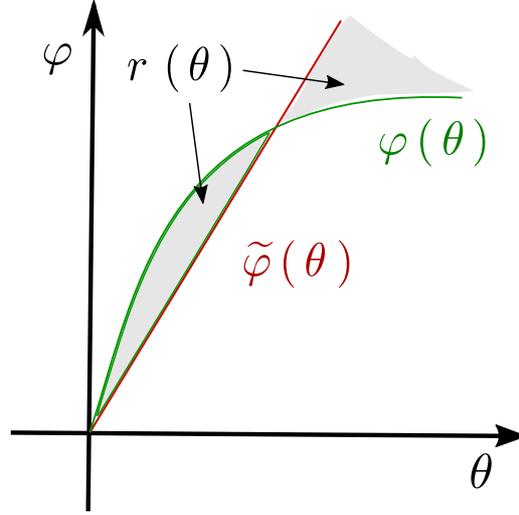
Figure 2: The schematic description of the functions $\varphi(\theta)$, $\widetilde{\varphi}(\theta)$ and $r(\theta)$.

Lastly, assuming that there is no liquid water coming from the ambient environment, for the moisture balance Equation (2.1) the boundary condition is expressed as:

$$
\mathbf{n} \cdot \left(D_\theta \cdot \frac{\partial \theta}{\partial x} + D_T \cdot \frac{\partial T}{\partial x} \right) = \frac{h_M \cdot M}{R_1} \cdot \varphi_\infty \cdot \left(\frac{P_{\text{sat}}}{T} - \frac{P_{\text{sat},\infty}}{T_\infty} \right)
$$

$$
+ \frac{h_M \cdot M}{R_1} \cdot \frac{P_{\text{sat}}}{T} \cdot \left(\frac{d\widetilde{\varphi}}{d\theta} \cdot \left(\theta - \theta_\infty \right) + r(\theta) \right), \quad \text{for } x = \{0, \ell\}. \quad (2.10)
$$

Using Equations (2.7) and (2.9), we obtain the boundary condition for the heat balance Equation (2.2):

$$
\mathbf{n} \cdot \left(k_T \cdot \frac{\partial T}{\partial x} + L_{12}^\circ \cdot k_{TM} \cdot \frac{\partial \theta}{\partial x} \right) = h_T \cdot \left(T - T_\infty \right) + L_{12}^\circ \cdot \frac{h_M \cdot M}{R_1} \cdot \varphi_\infty \cdot \left(\frac{P_{\text{sat}}}{T} - \frac{P_{\text{sat},\infty}}{T_\infty} \right)
$$

$$
+ L_{12}^\circ \cdot \frac{h_M \cdot M}{R_1} \cdot \frac{P_{\text{sat}}}{T} \cdot \left(\frac{d\widetilde{\varphi}}{d\theta} \cdot \left(\theta - \theta_\infty \right) + r(\theta) \right), \quad \text{for } x = \{0, \ell\}. \quad (2.11)
$$

Boundary conditions, considered in this section, represent the general overview. According to this results, any type of boundary conditions can be further derived, depending on the available data of heat and moisture transfer. In the next section, presented dimensionless formulation enables to solve whole class of such problems.

2.5   Dimensionless formulation

The governing equations together with boundary conditions are solved numerically in a dimensionless form. The solution in dimensionless formulation has advantages such as application to a class of problems sharing the same scaling parameters (*e.g.* FOURIER and BIOT numbers) [39, 40], simplification of a problem using asymptotic methods [41] and restriction of round-off errors.

For this purpose, the following dimensionless quantities are defined:

$$v \stackrel{\text{def}}{=} \frac{\theta}{\theta^\circ}, \qquad u \stackrel{\text{def}}{=} \frac{T}{T^\circ}, \qquad \varphi_\infty^\star \stackrel{\text{def}}{=} \frac{\varphi_\infty}{\varphi_\infty^\circ},$$

$$v_\infty \stackrel{\text{def}}{=} \frac{\theta_\infty}{\theta^\circ}, \qquad u_\infty \stackrel{\text{def}}{=} \frac{T_\infty}{T^\circ}, \qquad P_{\text{sat}}^\star \stackrel{\text{def}}{=} \frac{P_{\text{sat}}}{P_{\text{sat}}^\circ},$$

where the superscripts $^\circ$ and * represent a characteristic value of a dimensionless variable. Dimensionless quantities of space and time domains are:

$$x^\star \stackrel{\text{def}}{=} \frac{x}{\ell}, \qquad t^\star \stackrel{\text{def}}{=} \frac{t}{t^\circ}.$$

Material properties can be written in dimensionless form as follows:

$$D_\theta^\star \stackrel{\text{def}}{=} \frac{D_\theta}{D_\theta^\circ}, \qquad c_T^\star \stackrel{\text{def}}{=} \frac{c_T}{c_T^\circ}, \qquad k_{TM}^\star \stackrel{\text{def}}{=} \frac{k_{TM}}{k_{TM}^\circ}.$$

$$D_T^\star \stackrel{\text{def}}{=} \frac{D_T}{D_T^\circ}, \qquad k_T^\star \stackrel{\text{def}}{=} \frac{k_T}{k_T^\circ},$$

The FOURIER numbers are defined as:

$$\text{Fo}_M \stackrel{\text{def}}{=} \frac{t^\circ \cdot D_\theta^\circ}{\ell^2 \cdot \rho_2}, \qquad \text{Fo}_T \stackrel{\text{def}}{=} \frac{t^\circ \cdot k_T^\circ}{\ell^2 \cdot c_T^\circ}.$$

There are also dimensionless coupling parameters:

$$\gamma \stackrel{\text{def}}{=} \frac{D_T^\circ \cdot T^\circ}{D_\theta^\circ \cdot \theta^\circ}, \qquad \delta \stackrel{\text{def}}{=} L_{12}^\circ \cdot \frac{k_{TM}^\circ \cdot \theta^\circ}{k_T^\circ \cdot T^\circ}.$$

The BIOT numbers can be expressed as:

$$\text{Bi}_T^T \stackrel{\text{def}}{=} \frac{\ell \cdot h_T}{k_T^\circ},$$

$$\text{Bi}_M^{\text{sat}} \stackrel{\text{def}}{=} \frac{\ell \cdot \varphi_\infty^\circ \cdot h_M \cdot M}{D_\theta^\circ \cdot \theta^\circ \cdot R_1} \cdot \frac{P_{\text{sat}}^\circ}{T^\circ} \cdot \varphi_\infty^\star,$$

$$\text{Bi}_T^{\text{sat}} \stackrel{\text{def}}{=} L_{12}^\circ \cdot \frac{\ell \cdot \varphi_\infty^\circ \cdot h_M \cdot M}{k_T^\circ \cdot T^\circ \cdot R_1} \cdot \frac{P_{\text{sat}}^\circ}{T^\circ} \cdot \varphi_\infty^\star,$$

$$\text{Bi}_M^\theta \stackrel{\text{def}}{=} \frac{\ell \cdot h_M \cdot M}{D_\theta^\circ \cdot R_1} \cdot \frac{P_{\text{sat}}^\circ}{T^\circ} \cdot \frac{d\widetilde{\varphi}}{d\theta} \cdot \frac{P_{\text{sat}}^\star}{u},$$

$$\text{Bi}_T^\theta \stackrel{\text{def}}{=} L_{12}^\circ \cdot \frac{\ell \cdot \theta^\circ \cdot h_M \cdot M}{k_T^\circ \cdot T^\circ \cdot R_1} \cdot \frac{P_{\text{sat}}^\circ}{T^\circ} \cdot \frac{d\widetilde{\varphi}}{d\theta} \cdot \frac{P_{\text{sat}}^\star}{u}.$$

Finally, additional flux terms of the boundary conditions can be formulated as:

$$G_M \stackrel{\text{def}}{=} \frac{\ell \cdot r^\circ \cdot h_M \cdot M}{D_\theta^\circ \cdot \theta^\circ \cdot R_1} \cdot \frac{P_{\text{sat}}^\circ}{T^\circ} \cdot \frac{P_{\text{sat}}^\star}{u} \cdot r^\star(u),$$

$$G_T \stackrel{\text{def}}{=} L_{12}^\circ \cdot \frac{\ell \cdot r^\circ \cdot h_M \cdot M}{k_T^\circ \cdot T^\circ \cdot R_1} \cdot \frac{P_{\text{sat}}^\circ}{T^\circ} \cdot \frac{P_{\text{sat}}^\star}{u} \cdot r^\star(u),$$

where $r^\star(u)$ is the dimensionless formulation of the residual function $r(\theta)$.

For the model given in Equation (2.6), the equations representing mass $-v$ and heat $-u$ transfer in porous material can be written in the dimensionless form for $x^\star \in [0, 1]$ and $t^\star \in [0, \tau]$:

$$\frac{\partial v}{\partial t^\star} = \text{Fo}_M \cdot \frac{\partial}{\partial x^\star}\left(D_\theta^\star \cdot \frac{\partial v}{\partial x}\right) + \text{Fo}_M \cdot \gamma \cdot \frac{\partial}{\partial x^\star}\left(D_T^\star \cdot \frac{\partial u}{\partial x^\star}\right), \qquad (2.12a)$$

$$c_T^\star \cdot \frac{\partial u}{\partial t^\star} = \text{Fo}_T \cdot \frac{\partial}{\partial x^\star}\left(k_T^\star \cdot \frac{\partial u}{\partial x^\star}\right) + \text{Fo}_T \cdot \delta \cdot \frac{\partial}{\partial x^\star}\left(k_{TM}^\star \cdot \frac{\partial v}{\partial x^\star}\right). \qquad (2.12b)$$

The initial conditions at $t^\star = 0$ are $u_0 = v_0 = 1$ for $\forall x^\star \in [0, 1]$. The boundary conditions at the surface $x^\star = \{0, 1\}$ are defined as:

$$\mathbf{n} \cdot \left(D_\theta^\star \cdot \frac{\partial v}{\partial x} + \gamma \cdot D_T^\star \cdot \frac{\partial u}{\partial x^\star} \right) = \mathrm{Bi}_M^{\mathrm{sat}} \cdot \left(\frac{P_{\mathrm{sat}}^\star}{u} - \frac{P_{\mathrm{sat}, \infty}^\star}{u_\infty} \right)$$

$$+ \mathrm{Bi}_M^\theta \cdot \left(v - v_\infty \right) + G_M, \tag{2.13a}$$

$$\mathbf{n} \cdot \left(k_T^\star \cdot \frac{\partial v}{\partial x} + \delta \cdot k_{TM}^\star \cdot \frac{\partial u}{\partial x^\star} \right) = \mathrm{Bi}_T^T \cdot \left(u - u_\infty \right) + \mathrm{Bi}_T^{\mathrm{sat}} \cdot \left(\frac{P_{\mathrm{sat}}^\star}{u} - \frac{P_{\mathrm{sat}, \infty}^\star}{u_\infty} \right)$$

$$+ \mathrm{Bi}_T^\theta \cdot \left(v - v_\infty \right) + G_T. \tag{2.13b}$$

Henceforth, the presented formulation simplifies the description of case studies presented in Sections 4.1 and 4.2. For those sections, all necessary dimensionless values are given in appendices. The next section presents two numerical methods applied in the studies. The section starts with the descriptions of a discretization for a simple diffusion equation. However, both methods are presented with extensions to the coupled and nonlinear equations. At the end of the section, definitions of criteria to evaluate a numerical efficiency of methods are provided.

3   Numerical Methods

Initial-boundary value problem, namely simple diffusion equation [5] in one dimension, is considered in order to explain numerical schemes. For the sake of simplicity and without losing generality all other terms of the dimensionless Equations (2.12) are dropped out.

$$\frac{\partial u}{\partial t} = \frac{\partial}{\partial x} \left(d \cdot \frac{\partial u}{\partial x} \right), \tag{3.1}$$

where d is the material diffusivity, $u(x, t = 0) \overset{\mathrm{def}}{:=} u_0(x)$ is the initial condition, $u(x = 0, t) \overset{\mathrm{def}}{:=} u_\infty^L(t)$ and $u(x = 1, t) \overset{\mathrm{def}}{:=} u_\infty^R(t)$ are DIRICHLET boundary conditions for the left and right boundaries.

In order to describe the numerical schemes, let us consider the following discretization for the space and time domains [42]. Uniform discretization of the space interval $\Omega_x \rightsquigarrow \Omega_h$ is written as:

$$\Omega_h = \bigcup_{j=1}^{N_x} [x_j, x_{j+1}], \quad x_{j+1} - x_j \equiv \Delta x, \ \forall j \in \{1, \ldots, N_x\}.$$

Time layers are spaced uniformly as well:

$$t^n = n \Delta t, \quad \Delta t = \mathrm{const} > 0, \ \forall n \in \{0, \ldots, N_t\}.$$

The discretization error depends on the choice of parameters N_x and N_t. These values can be chosen according to the computational cost requirements. The points of the (x, t) plane, where $x = x_j$ and $t = t^n$ intersect are called *mesh points* or nodes of the grid. The approximate solution of Equation (3.1) will be defined only at the grid nodes. The values of the function $u(x, t)$ at discrete nodes are denoted by $u_j^n := u(x_j, t^n)$.

10

3.1 The Du Fort–Frankel Method

The improved explicit method, called DU FORT–FRANKEL, is one of the methods which can be used to find the numerical solution of the problems such as Equation (3.1). The method was first presented in the listed works [43–45] almost 50 years ago. In this article, the detailed discretization of the scheme is omitted, and interested readers can refer to the recent papers [26, 27]. There the method has been extended for coupled equations of heat and mass transfer, and its performance has been discussed in more details.

The value of u_j^{n+1} with DU FORT–FRANKEL (DF) discretization can be expressed in the following form for the linear case:

$$u_j^{n+1} = \frac{1 - \alpha}{1 + \alpha} \cdot u_j^{n-1} + \frac{\alpha}{1 + \alpha} \cdot \left(u_{j+1}^n + u_{j-1}^n \right), \qquad n \geqslant 1,$$

where the coefficient α is expressed as

$$\alpha \overset{\text{def}}{=} 2 \frac{\Delta t}{\Delta x^2} \cdot k.$$

The extension of the DF scheme for a nonlinear case, where the nonlinearity comes from the material diffusivity k, can be written in the following way:

$$u_j^{n+1} = \frac{\alpha_0 - \alpha_3}{\alpha_0 + \alpha_3} \cdot u_j^{n-1} + \frac{\alpha_1}{\alpha_0 + \alpha_3} \cdot u_{j+1}^n + \frac{\alpha_2}{\alpha_0 + \alpha_3} \cdot u_{j-1}^n, \qquad n \geqslant 1,$$

where

$$\alpha_0 \overset{\text{def}}{=} 1, \qquad\qquad \alpha_2 \overset{\text{def}}{=} 2 \frac{\Delta t}{\Delta x^2} \cdot k_{j-\frac{1}{2}}^n,$$

$$\alpha_1 \overset{\text{def}}{=} 2 \frac{\Delta t}{\Delta x^2} \cdot k_{j+\frac{1}{2}}^n, \qquad \alpha_3 \overset{\text{def}}{=} \frac{\Delta t}{\Delta x^2} \cdot \left(k_{j+\frac{1}{2}}^n + k_{j-\frac{1}{2}}^n \right).$$

It should be noted that the material diffusivity can be expressed explicitly at $j \pm \frac{1}{2}$ for the time-step t^n:

$$k_{j\pm\frac{1}{2}}^n = k \left(\frac{u_{j\pm 1}^n + u_j^n}{2} \right). \tag{3.2}$$

The stencil of the DF method is illustrated in Figure 3a.

3.2 The Super–Time–Stepping Method

Super–Time–Stepping (STS) approach was first presented in the work of GENTZSCH [18] almost 40 years ago for parabolic problems. The method itself belongs to a class of RUNGE–KUTTA-like methods, which iterative algorithms admit some kind of temporal interpretation. It was claimed to remarkably speed up the explicit time–stepping schemes in a very simple way. However, despite its obvious advantages, since then the method was only employed for a limited range of problems. The notable applications to linear and nonlinear parabolic problems were performed in [23–25]. In the works of ALEXIADES [24, 25], the method was inspired by the recursion relations associated with the CHEBYSHEV polynomials. The STS method was then further developed by MEYER *et al.* [20, 21] by introducing the methods based on the recursion relations of the shifted LEGENDRE polynomials. The properties of both polynomials allow ensuring the
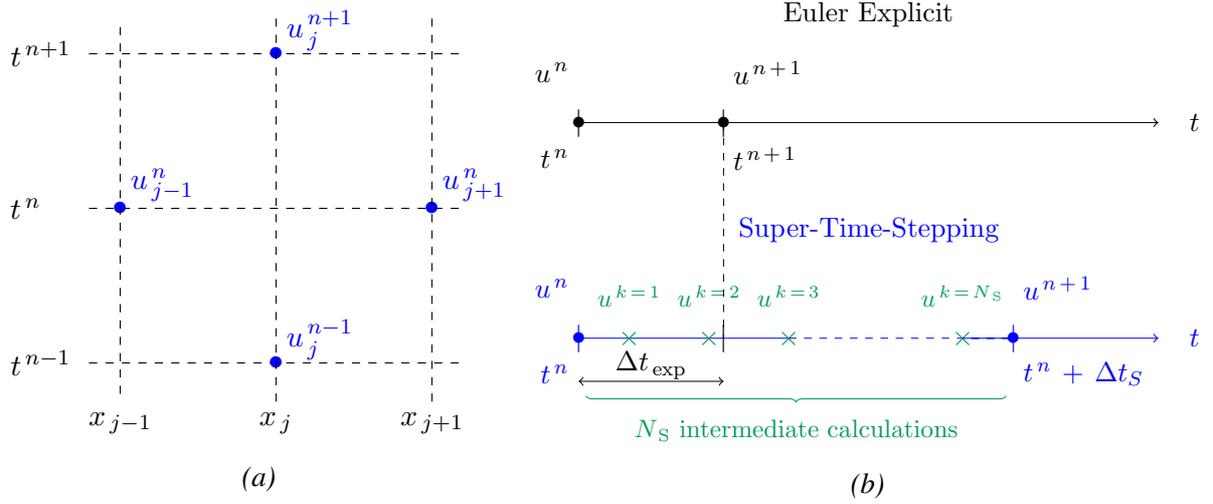
11

Figure 3: Stencils of DU FORT–FRANKEL *scheme (a) and Super–Time–Stepping method in comparison with* EULER *explicit scheme (b).*

stability of the method at the end of each iteration stage. Thereby, the schemes are able to relax the strong stability requirement at the end of every time-step [25].

In this work, it was proved that the STS method can be more efficient than the well-known EULER schemes of the order $\mathcal{O}\left(\Delta t + \Delta x^2\right)$ in application to the building physics phenomena. There are two main benefits to the STS method. Firstly, compared to the EULER explicit scheme, the STS method may overcome the stability condition of COURANT–FRIEDRICHS–LEWY (CFL) [46] written for Equation (3.1):

$$\Delta t \leqslant \frac{1}{2\,k} \cdot \Delta x^2 \,. \tag{3.3}$$

This condition imposes certain restrictions for the application of the EULER explicit scheme into building simulation tools [27]. Secondly, compared to EULER implicit scheme, the STS methods are much easier to implement, since it has an explicit formulation. Indeed, the implicit scheme is unconditionally stable, but it requires a relatively high number of sub-iterations to handle with nonlinearity. Therefore, while maintaining high accuracy, the STS method makes it possible to implement the discretization with larger time-steps and to reduce computational time requirement.

The general idea of the method, very well described in the work of ALEXIADES [25], is given below. Also, in this article, three STS approaches are considered based on three families of orthogonal polynomials, namely shifted CHEBYSHEV polynomial of degree N_S, and two shifted LEGENDRE polynomials of first and second orders. Without loss of generality and for simplicity of presentation, we consider the time-dependent linear diffusion Equation (3.1). The EULER explicit discretization for this equation can be written as [25]:

$$u^{n+1} = \left(\mathbf{I} - \Delta t \cdot \mathbf{A}\right) \cdot u^n, \quad n \geqslant 0, \tag{3.4}$$

where matrix $\mathbf{A}$ can be constructed according to the chosen space discretization. For example, using central finite differences discretization, the matrix $\mathbf{A}$ is a symmetric, positive definite matrix which can be expressed in the following way in the case of linear parameter k and DIRICHLET

boundary conditions:

$$\mathbf{A} \stackrel{\text{def}}{=} \alpha \cdot \begin{pmatrix} 2 & -1 & & 0 \\ -1 & \ddots & \ddots & \\ & \ddots & \ddots & -1 \\ 0 & & -1 & 2 \end{pmatrix}, \tag{3.5}$$

where

$$\alpha \stackrel{\text{def}}{=} \frac{k}{\Delta x^2}.$$

The stability condition of the scheme is associated with the spectral radius ρ of the matrix operator:

$$\rho\left(\mathbf{I} - \Delta t \cdot \mathbf{A}\right) < 1,$$

where the spectral radius operator $\rho\left(-\right)$ is traditionally defined as follows:

$$\rho : \operatorname{Mat}_{m \times m}(\mathbb{R}) \longrightarrow \mathbb{R}_{\geqslant 0},$$

$$\operatorname{Mat}_{m \times m} \ni A \longmapsto \max_{1 \leqslant j \leqslant m}\left\{|\lambda_j| \,\middle|\, A v_j = \lambda_j v_j, \, v_j \in \mathbb{R}^m \setminus \mathbf{0}\right\} \in \mathbb{R}_{\geqslant 0}.$$

Noting the maximum eigenvalue of matrix $\mathbf{A}$ as $\lambda_{\max}$, the above relationship yields to the following stability condition for time discretization ([25]):

$$|1 - \Delta t \cdot \lambda_{\max}| < 1 \quad \Longrightarrow \quad \Delta t < \Delta t_{\exp}, \tag{3.6}$$

with

$$\Delta t_{\exp} \stackrel{\text{def}}{=} \frac{2}{\lambda_{\max}}, \tag{3.7}$$

where $\lambda_{\max} = \dfrac{4k}{\Delta x^2}$. The above condition (3.6) can be relaxed by the STS method. The main advantage of the method is that it allows relaxing the stability constraint on each time-step Δt by introducing superstep Δt_{S}. The STS imposes stability constraint only at the end of a cycle of N_{S} time-steps, which leads to a method similar to a RUNGE–KUTTA-like method with N_{S} stages. This technique can be better understood with the stencils of the STS scheme in Figure 3b. One can observe that the STS method performs sequences of N_{S} inner steps (intermediate calculations) and in general executes $N_{\mathrm{S}} \cdot \dfrac{\tau}{\Delta t_{\mathrm{S}}}$ explicit steps, where τ is the total simulation time. As a result, approximately $N_{\mathrm{STS}} \stackrel{\text{def}}{=} \dfrac{\tau}{\Delta t_{\mathrm{S}}}$ temporal nodes are obtained.

The definition of superstep is different for the schemes with CHEBYSHEV and LEGENDRE polynomials. Nonetheless, according to [25], the stability condition (3.6) can be written as:

$$\left| \mathsf{P}_{N_{\mathrm{S}}}\left(\Delta t_S, \lambda\right) \right| \leqslant 1, \quad \forall \lambda \in [\lambda_{\min}, \lambda_{\max}], \tag{3.8}$$

where $\lambda_{\min} > 0$ is the smallest eigenvalue of the matrix $\mathbf{A}$ (3.5). Hence, the supersteps Δt_{S} for all three polynomials can be chosen according to the number of time-substeps N_{S} and explicit time-step $\Delta t_{\exp}$ defined in (3.7):

- **RKC1**: RUNGE–KUTTA–CHEBYSHEV method [25]:

$$\Delta t_{\mathrm{S}} = \sum_{k=1}^{N_{\mathrm{S}}} \tau_k \xrightarrow{\lambda_{\max}} N_{\mathrm{S}}^2 \cdot \Delta t_{\exp}, \tag{3.9}$$

where τ_k – the time-step of intermediary stage k, presented later in the Section 3.2.1.

13

- **RKL1**: RUNGE–KUTTA–LEGENDRE method of the first order [20]:

$$\Delta t_{\mathrm{S}} \;\leqslant\; \frac{N_{\mathrm{S}}^2 \,+\, N_{\mathrm{S}}}{2} \cdot \Delta t_{\exp}. \tag{3.10}$$

- **RKL2**: RUNGE–KUTTA–LEGENDRE method of the second order [20]:

$$\Delta t_{\mathrm{S}} \;\leqslant\; \frac{N_{\mathrm{S}}^2 \,+\, N_{\mathrm{S}} \,-\, 2}{4} \cdot \Delta t_{\exp}. \tag{3.11}$$

Lastly, one can express discretization (3.4) [25] in terms of discrete evolution operator:

$$u^{n+1} \;=\; \left(\mathsf{P}_N\big(\Delta t_{\mathrm{S}}, \mathbf{A}\big)\right) \cdot u^n, \quad n \,=\, 0, 1, \dots N_{STS}. \tag{3.12}$$

In the next sections, broader discussions with examples of algorithms are presented for RKC1, RKL1 and RKL2. For any further details, interested readers can refer to [20, 21, 24, 25].

3.2.1 RKC1: RUNGE–KUTTA–CHEBYSHEV method

Within this approach, according to [25], a stability polynomial can be written, with the λ – eigenvalues of the matrix $\mathbf{A}$, as follows:

$$\mathsf{P}_{N_{\mathrm{S}}}\big(\tau_k, \lambda\big) \stackrel{\text{def}}{:=} \prod_{k\,=\,1}^{N_{\mathrm{S}}} \big(1 \,-\, \tau_k \cdot \lambda\big), \qquad \forall\, \lambda \,\in\, [\,\lambda_{\min}, \lambda_{\max}\,].$$

In addition, the optimal properties of CHEBYSHEV polynomials $\mathsf{T}_N(\cdot)$ [47] allow to reformulate the stability condition (3.8) as:

$$\left|\,\mathsf{P}_{N_{\mathrm{S}}}\big(\tau_k, \lambda\big)\,\right| \;\leqslant\; K < 1,$$

for

$$K \;=\; \mathsf{T}_{N_{\mathrm{S}}}\left(\frac{\lambda_{\max} \,+\, \mu}{\lambda_{\max} \,-\, \mu}\right),$$

where μ is a number in the interval $(\,0, \lambda_{\min}\,]$. Thereby, a modified version of condition (3.6) can be written as:

$$\left|\prod_{k\,=\,1}^{N_{\mathrm{S}}} \big(1 \,-\, \tau_k \cdot \lambda\big)\right| \;<\; 1, \qquad \forall\, \lambda \,\in\, [\,\lambda_{\min}, \lambda_{\max}\,],$$

where τ_k is explicitly defined as:

$$\tau_k \;=\; \Delta t_{\exp} \cdot \left[\left(-1 \,+\, \nu\right) \cdot \cos\!\left(\frac{2k \,-\, 1}{N_{\mathrm{S}}} \cdot \frac{\pi}{2}\right) \,+\, \nu \,+\, 1\right]^{-1}, \tag{3.13}$$

for $k \,=\, 1, \dots, N_{\mathrm{S}}$ and $\nu \stackrel{\text{def}}{:=} \dfrac{\mu}{\lambda_{\max}}$. Hence, by the RKC1 approach, one can find the explicit value of Δt_{S} and define a new algorithm based on Equation (3.4):

$$u^{n+1} \;=\; \left(\prod_{k\,=\,1}^{N} \big(\mathbf{I} \,-\, \tau_k \cdot \mathbf{A}\big)\right) \cdot u^n, \quad n \,=\, 0, 1, \dots N_{STS}.$$

The algorithm of the RKC1 scheme can be summarized in the following way:

Set $N_S \geqslant 1$;
Set $\mu > 0$;
Compute τ_k according to the Formula (3.13), $\forall k = 1, \dots, N_S$;
Compute $\Delta t_S = \sum_{k=1}^{N_S} \tau_k$;
while $t \leqslant T$ **do**
$\quad$ **for** $k = 1, \dots, N_S$ **do**
$\quad\quad$ | $u^k = u^{k-1} - \tau_k \cdot \mathbf{A} \cdot u^{k-1}$
$\quad$ **end**
$\quad$ $t = t + \Delta t_S$;
$\quad$ $u^0 = u^{N_S}$;
end

Algorithm 1: *The algorithm of the RKC1 scheme.*

3.2.2 RKL: RUNGE–KUTTA–LEGENDRE approach

The STS method based on LEGENDRE'S polynomials has a different approach from the RKC1 method. The main difference is that the superstep Δt_S is defined by the user. The explanation of the approach, according to [20], starts with a demonstration of the first order scheme RKL1 and, then, follows with the second order scheme RKL2.

The RKL1 scheme can be written in the following way:

$$
\begin{aligned}
u^0 &= u(t^n), &(3.14)\\
u^1 &= u^0 + \tilde{\mu}_1 \cdot \Delta t_S \cdot \mathbf{A} \cdot u^0,\\
u^k &= \mu_k \cdot u^{k-1} + \nu_k \cdot u^{k-2} + \tilde{\mu}_k \cdot \Delta t_S \cdot \mathbf{A} \cdot u^{k-1}, \quad 2 \leqslant k \leqslant N_S,\\
u(t^n + \Delta t_S) &= u^{N_S}.
\end{aligned}
$$

with the parameters:

$$
\mu_k = \frac{2k-1}{k}, \qquad \nu_k = \frac{k-1}{k}, \qquad \tilde{\mu}_k = \frac{2k-1}{k} \cdot \frac{2}{N_S^2 + N_S}.
$$

In a similar way, the RKL2 scheme can be written as follows:

$$
\begin{aligned}
u^0 &= u(t^n), &(3.15)\\
u^1 &= u^0 + \tilde{\mu}_1 \cdot \Delta t_S \cdot \mathbf{A} \cdot u^0,\\
u^k &= \mu_k \cdot u^{k-1} + \nu_k \cdot u^{k-2} + (1 - \mu_k - \nu_k) \cdot u^0 +\\
&\quad \tilde{\mu}_k \cdot \Delta t_S \cdot \mathbf{A} \cdot u^{k-1} + \tilde{\gamma}_k \cdot \Delta t_S \cdot \mathbf{A} \cdot u^0, \quad 2 \leqslant k \leqslant N_S,\\
u(t^n + \Delta t_S) &= u^{N_S},
\end{aligned}
$$

where

$$
b_k = \frac{k^2 + k - 2}{2k \cdot (k+1)}, \qquad \nu_k = \frac{k-1}{k} \cdot \frac{b_k}{b_{k-2}}, \qquad a_k = 1 - b_k,
$$

$$
\mu_k = \frac{2k-1}{k} \cdot \frac{b_k}{b_{k-1}}, \qquad \tilde{\mu}_k = 4\frac{2k-1}{k \cdot (N_S^2 + N_S - 2)} \cdot \frac{b_k}{b_{k-1}}, \qquad \tilde{\gamma}_k = -a_{k-1} \cdot \tilde{\mu}_k.
$$

The algorithm of the RKL (1, 2) schemes can be summarized in the following Algorithm (2):

Set $N_S \geqslant 2$;
Compute Δt_S ; (according to the Formulas (3.10) or (3.11)) ;
while $t \leqslant T$ **do**

$\quad u^1 = u^0 + \tilde{\mu}_1 \cdot \Delta t_S \cdot \mathbf{A} \cdot u^0$;

$\quad$ **for** $k = 2, \ldots, N_S$ **do**

$\quad\quad u^k = f\left(u^{k-1}, \mu_k, \Delta t_S, \ldots\right)$ (using (3.14) or (3.15))

$\quad$ **end**

$\quad t = t + \Delta t_S$;

$\quad u^0 = u^{N_S}$;

end

Algorithm 2: *The algorithm of the RKL (1, 2) approach.*

3.2.3 Extension to nonlinear equation

The extension of the method to the nonlinear case, where the material diffusivity k is a dependent variable of a grid function $U^n = \left\{ u_j^n \right\}_{j=1}^{N_x}$, can be expressed with the change of the matrix $\mathbf{A}$ at (3.5). The matrix now depends on all values of a grid function, *i.e.* $\mathbf{A}\left(U^n\right)$, and can be written in the following form:

$$\mathbf{A}\left(U^n\right) \overset{\text{def}}{:=} \alpha \cdot \begin{pmatrix} \left(k_{j+\frac{1}{2}}^n + k_{j-\frac{1}{2}}^n\right) & -k_{j+\frac{1}{2}}^n & & 0 \\ -k_{j-\frac{1}{2}}^n & \ddots & \ddots & \\ & \ddots & \ddots & -k_{j+\frac{1}{2}}^n \\ 0 & & -k_{j-\frac{1}{2}}^n & \left(k_{j+\frac{1}{2}}^n + k_{j-\frac{1}{2}}^n\right) \end{pmatrix},$$

where

$$\alpha \overset{\text{def}}{:=} \frac{1}{2\Delta x^2}$$

and $k_{j \pm \frac{1}{2}}^n$ can be computed with the Equality (3.2).

This superstep Δt_S should be computed with formulas (3.9) – (3.11). It can be seen that these values should be estimated in accordance with $\Delta t_{\exp}$ which is directly linked with CFL stability condition. However, a value of the CFL condition is not known *a priori*, hence needs to be estimated. For the simple diffusion Equation (3.1), $\Delta t_{\exp}$ can be chosen according to the following restriction:

$$\Delta t_{\exp} \leqslant \frac{\Delta x^2}{2} \cdot \min_{\left\{u_\infty^L(t),\, u_\infty^R(t)\right\}} \left\{ \frac{1}{k\left(u_\infty^L\right)}, \frac{1}{k\left(u_\infty^R\right)} \right\}.$$

It can also be mentioned that the above expression is totally reasonable for the case when nonlinear parameter $k(u)$ is a monotone increasing function. Moreover, imposing boundary conditions ensure that $u < \max_{t \geqslant 0} \left\{ u_\infty^L(t), u_\infty^R(t) \right\}$ always holds. Hence, it is also true that $k(u) < \max_{t \geqslant 0} \left\{ k\left(u_\infty^L\right), k\left(u_\infty^R\right) \right\}$. So, the relationship $\frac{1}{k(u)} < \min_{t \geqslant 0} \left\{ \frac{1}{k\left(u_\infty^L\right)}, \frac{1}{k\left(u_\infty^R\right)} \right\}$ always holds true as well.

3.2.4 Extension to coupled system of nonlinear equations

The discretization by the STS method for the case of equations' system can be written in the same way as Equation (3.12) but with vector notation:

$$\mathbf{u^{k+1}} = \mathsf{P}_{N_\mathrm{S}}\big(\Delta t_\mathrm{S},\, \mathbf{A}\big) \cdot \mathbf{u^k},\tag{3.16}$$

where $\mathbf{u} \stackrel{\mathrm{def}}{:=} \big(u_1,\, u_2,\, \ldots,\, u_n\big)$ – a vector, which includes all n variables, $\mathbf{A}$ is the discretization matrix and Δt_S is the super-time-step.

As was mentioned earlier, a value of the CFL condition is not known, therefore for the dimensionless coupled Equations (2.12) $\Delta t_\mathrm{exp}^\star$ can be computed from the extremal values of $u_\infty^{L,R}$ and $v_\infty^{L,R}$. Those values are given for the boundary conditions (2.13a) and (2.13b) at $x^\star = 0$ and $x^\star = 1$, which correspond to left (L) and right (R) boundary conditions respectively (see, for example, Figure 1). For the dimensionless mass balance Equation (2.12a) the value of $\Delta t_\mathrm{exp}^\star$ should be:

$$\Delta t_\mathrm{exp}^{\star M} \leqslant \frac{\left(\Delta x^\star\right)^2}{2}\, \min\left\{ \min_{v_\infty^{L,R},\, u_\infty^{L,R}} \left(\frac{1}{\mathrm{Fo}_M \cdot D_\theta^\star\left(v_\infty^{L,R},\, u_\infty^{L,R}\right)}\right), \right.$$
$$\left. \min_{v_\infty^{L,R},\, u_\infty^{L,R}} \left(\frac{1}{\mathrm{Fo}_M \cdot \gamma \cdot D_T^\star\left(v_\infty^{L,R},\, u_\infty^{L,R}\right)}\right)\right\},$$

and for heat balance Equation (2.12b):

$$\Delta t_\mathrm{exp}^{\star T} \leqslant \frac{\left(\Delta x^\star\right)^2}{2}\, \min\left\{ \min_{v_\infty^{L,R},\, u_\infty^{L,R}} \left(\frac{c_T^\star\left(v_\infty^{L,R},\, u_\infty^{L,R}\right)}{\mathrm{Fo}_T \cdot k_T^\star\left(v_\infty^{L,R},\, u_\infty^{L,R}\right)}\right), \right.$$
$$\left. \min_{v_\infty^{L,R},\, u_\infty^{L,R}} \left(\frac{c_T^\star\left(v_\infty^{L,R},\, u_\infty^{L,R}\right)}{\mathrm{Fo}_T \cdot \delta \cdot k_{TM}^\star\left(v_\infty^{L,R},\, u_\infty^{L,R}\right)}\right)\right\}.$$

From these two results, the minimum should be chosen as:

$$\Delta t_\mathrm{exp}^\star \leqslant \min\left\{\Delta t_\mathrm{exp}^{\star M},\, \Delta t_\mathrm{exp}^{\star T}\right\}.\tag{3.17}$$

3.3 Comparing numerical solutions

Numerical methods can be compared among each other by computing the $\mathcal{L}_2$ error [42] between a numerical solution u_num and a reference solution u_ref:

$$\varepsilon_2(x) \stackrel{\mathrm{def}}{:=} \big\|\,u_\mathrm{ref}(x,t) - u_\mathrm{num}(x,t)\,\big\|_2$$
$$= \sqrt{\frac{1}{N_t}\sum_{j=1}^{N_t}\Big(u_{j,\mathrm{ref}}(x,t_j) - u_{j,\mathrm{num}}(x,t_j)\Big)^2},$$

where N_t is the total number of temporal steps. For the numerical validation, the reference solution is taken to be equal to the pseudo-spectral solution. This solution is obtained with the `Matlab` open source package `Chebfun` [48], which is based on the CHEBYSHEV polynomials adaptive spectral methods. Likewise, the Significant Correct Digits of a solution can be computed as [49]:

$$\mathrm{scd}(u) \stackrel{\mathrm{def}}{:=} -\log_{10}\left\|\frac{u_\mathrm{num}(x,\tau) - u_\mathrm{ref}(x,\tau)}{u_\mathrm{ref}(x,\tau)}\right\|_\infty.$$

To evaluate the *fidelity* of the numerical methods, the observed data from experimental set up is taken instead of the reference solution u_{ref}. One can refer to the fidelity as a quantitative measure to evaluate the ability of the numerical approximations with the governing equations to reproduce the observed data [16, 17]. The stability, accuracy and, later, the fidelity of the numerical models is quantified with the global uniform error $\mathcal{L}_{\infty}$, which is defined as:

$$\varepsilon_{\infty} \overset{\mathrm{def}}{:=} \sup_{x \in \left[\, 0,\, \ell \,\right]} \varepsilon_{2}\left(\, x \,\right). \tag{3.18}$$

The relative error, evaluated at the point $x \;=\; x_{0}$, is also discussed for some cases:

$$\eta\left(\, t \,\right) \overset{\mathrm{def}}{:=} \frac{\left|\, u_{\mathrm{ref}}\left(\, x_{0},\, t \,\right) \;-\; u_{\mathrm{num}}\left(\, x_{0},\, t \,\right) \,\right|}{u_{\mathrm{ref}}\left(\, x_{0},\, t \,\right)},$$

where $\left|\, u_{\mathrm{ref}}\left(\, x_{0},\, t \,\right) \;-\; u_{\mathrm{num}}\left(\, x_{0},\, t \,\right) \,\right|$ is the residual.

In order to determine whether numerical results over or under predict the experimental data, the distribution function f is used in Section 5. The mean E, or expected value of the distribution function, is calculated as another assessment of a simulation error.

The efficiency of DU FORT–FRANKEL and Super–Time–Stepping methods are also compared relatively to the EULER explicit scheme. For this purpose, two ratios are introduced. The first one is the ratio of the total number of temporal steps $\varrho_{N_{t}}\left[\,\%\,\right]$, which is computed as follows:

$$\varrho_{N_{t}} \overset{\mathrm{def}}{:=} \frac{N_{t}^{\mathrm{scheme}}}{N_{t}^{\mathrm{EULER}}} \cdot 100\%,$$

where N_{t}^{scheme} and N_{t}^{EULER} are the total numbers of temporal steps of the DF or STS schemes and of the EULER explicit scheme respectively. The second ratio, $\varrho_{\mathrm{CPU}}\left[\,\%\,\right]$, shows how computational cost can be shortened compared to the EULER explicit scheme:

$$\varrho_{\mathrm{CPU}} \overset{\mathrm{def}}{:=} \frac{t_{\mathrm{CPU}}^{\mathrm{scheme}}}{t_{\mathrm{CPU}}^{\mathrm{EULER}}} \cdot 100\%,$$

where $t_{\mathrm{CPU}}^{\mathrm{scheme}}\left[\,\mathsf{s}\,\right]$ and $t_{\mathrm{CPU}}^{\mathrm{EULER}}\left[\,\mathsf{s}\,\right]$ are computational times required by the DF or STS schemes and by the EULER explicit scheme respectively. For a long-term simulation, one can also calculate the computational time ratio per day $\varrho_{\mathrm{CPU}}^{\mathrm{day}}\left[\,\mathsf{s/d}\,\right]$, which evaluates how many computational seconds are required to perform the simulation for one day:

$$\varrho_{\mathrm{CPU}}^{\mathrm{day}} \overset{\mathrm{def}}{:=} \frac{t_{\mathrm{CPU}}^{\mathrm{scheme}}}{\tau / \left(\, 24\,\mathsf{h} \,\right)},$$

where $\tau\left[\,\mathsf{h}\,\right]$ is the final time.

Above-mentioned quantities are used to evaluate numerical methods. In the following section, the methods are validated for two case studies.

4 Numerical validation

4.1 First case: linear heat and mass transfer model

For the first case, material properties are considered to be constant throughout the material and independent of the physical conditions and the environment of studied material. The model is taken in its dimensionless form as (2.12) together with the initial and boundary conditions (2.13).
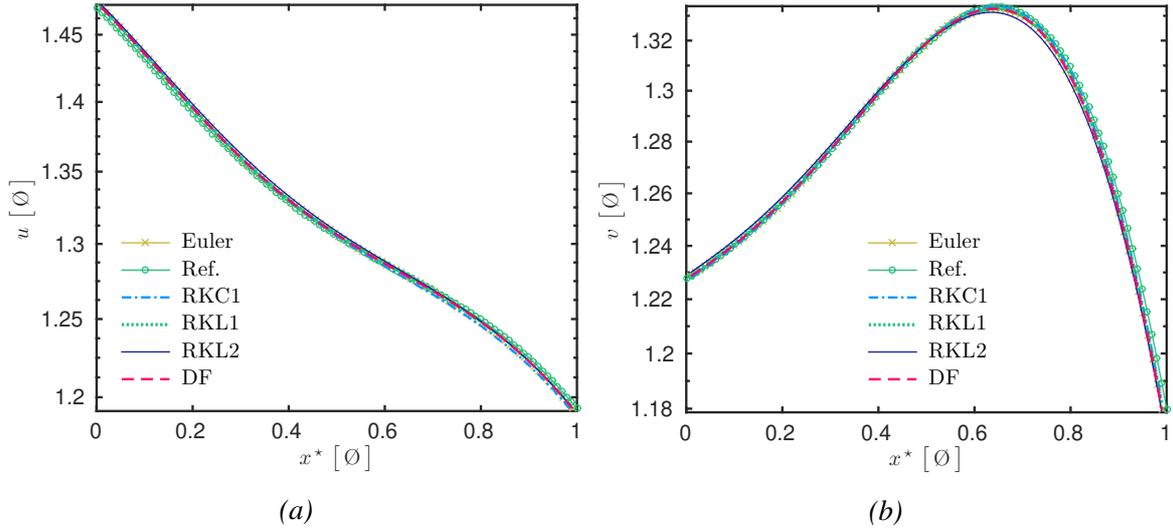
Figure 4: *Dimensionless* u *(a) and* v *(b) profiles at full time discretization, for* $\Delta t^\star$ *values presented in Table* 1 *and* $\Delta x^\star = 10^{-2}$.

4.1.1 Case study

Dimensionless parameters are presented in Appendix A.1. The total simulation time is $\tau^\star = 24$. The space discretization parameter is $\Delta x^\star = 10^{-2}$ for all schemes. The value of the time-step parameter for each scheme is discussed below on the case by case basis.

4.1.2 Results and discussion

For the sake of simplicity and without loss of generality, the results have been presented in their dimensionless form. Profiles of dimensionless temperature – u and moisture content – v at final state are presented in Figure 4. It can be seen that simulation results of all methods are very close to the reference solution (for a reference solution see Section 3.3). The steady decrease in temperature and slight fluctuation of moisture content can be noticed in the figures. Another good correspondence of the results can be seen in Figure 5 for profiles in the middle of the material. Distribution of heat and moisture starts from initial values (which are equal to 1 in the dimensionless representation), and shows time fluctuations according to the periodic boundary conditions.

The parametric study of schemes, *i.e.* the accuracy with respect to the discretization parameter Δt, is presented by plotting results of the $\mathcal{L}_\infty$ error as a function of $\Delta t^\star$ in Figure 6. In this article, the main interest is on a comparison of predictions with the DF and STS schemes. Therefore, a parametric study of the EULER explicit scheme is omitted, as it was already discussed in the literature in comparison with DU FORT–FRANKEL scheme. Interested readers may consult these previous results in [26, 27]. From Figure 6 one can see that the $\mathcal{L}_\infty$ error of the STS methods is high for small values of Δt. Basically, the error between two orange dashed lines, show that the STS methods "prefers" time-steps bigger than Δt_{CFL}, required for stability of the EULER explicit scheme in accordance with the CFL condition 3.3. As the STS methods were designed to overcome that stability restriction by "jumping" with bigger time-steps, the number of supersteps N_S should always be higher than one for RKC1 and two for RKL methods. However, the choice of N_S and, consequently, of Δt_S has to be done with caution. These observations are also consistent with those of MEYER *et al.* [20, 21]. Further study for the influence of N_S choice is discussed
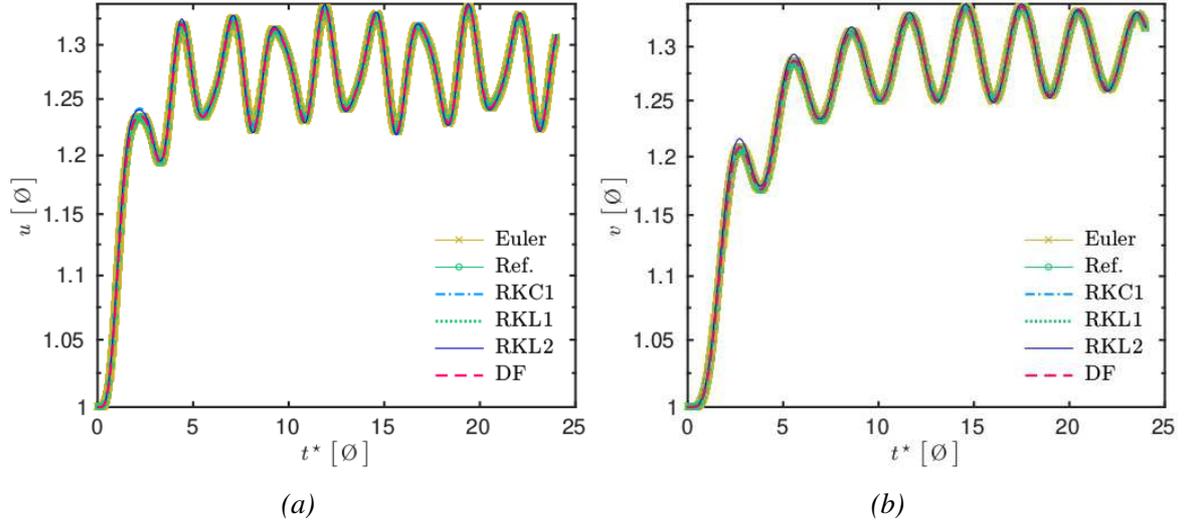
19

Figure 5: Dimensionless u (a) and v (b) evolutions at $x^\star = 0.5$, for $\Delta t^\star$ values presented in Table 1 and $\Delta x^\star = 10^{-2}$.

later in this section.

Generally, the results of the STS methods hold the tolerable level of an engineering accuracy up to $\Delta t = 10^{-1}$. In comparison with the DF scheme, a comparable level of error can be obtained with bigger time-steps. This again shows the possible effectiveness of the STS methods to solve problems for coarser time discretization. Moreover, it should be noted that the DF method is intrusive, while the STS methods are non–intrusive. Indeed, the DF method is fully discrete, *i.e.* it is a discretization in both space and time domains. Whereas the STS methods can be coupled with any space discretization solvers without any problem, *i.e.* the methods do not depend on an operator. This aspect of the STS methods shall be highly beneficial for further employment on two-dimensional heat and mass transfer models.

One can also observe that the convergence of the DF method follows the second order accuracy, while for the STS methods there are unexpected results. The RKC1 and RKL1 methods follow the first order accuracy, which proves their applicability and the construction of schemes. However, the RKL2 method does not follow the second order accuracy in accordance with the order of LEGENDRE polynomial used for the construction of the scheme. This observation questions the reliability of the RKL2 method as it apparently does not follow its convergence path. Hence, the application of this scheme is questioned for further studies.

On the Table 1 a comparison of the numerical results for all approaches is displayed. The relative effectiveness of the methods compared to the EULER explicit scheme is also given. One can see that with the STS methods it is possible to obtain an $\mathcal{L}_\infty$ error of order 10^{-3} with time-steps almost 100 times bigger than it is required with classical stability restrictions. Another advantage of the STS method is seen from the ratios ϱ_{N_t}, which are only 1%, 1.8% and 3.7% with the RKC1, RKL1 and RKL2 schemes respectively. From the table, it can also be noted that the digits accuracy (SCD) is more than two for all schemes, which basically means that differences in the results occur only in the third digit. Also, Figure 7 displays the $\mathcal{L}_2$ error between the numerical simulation results and reference solution, for $\Delta t^\star$ presented in Table 1 and $\Delta x^\star = 10^{-2}$. The consistency between results is observed, thus for the purpose of validation, these results prove the accuracy of the implemented methods.

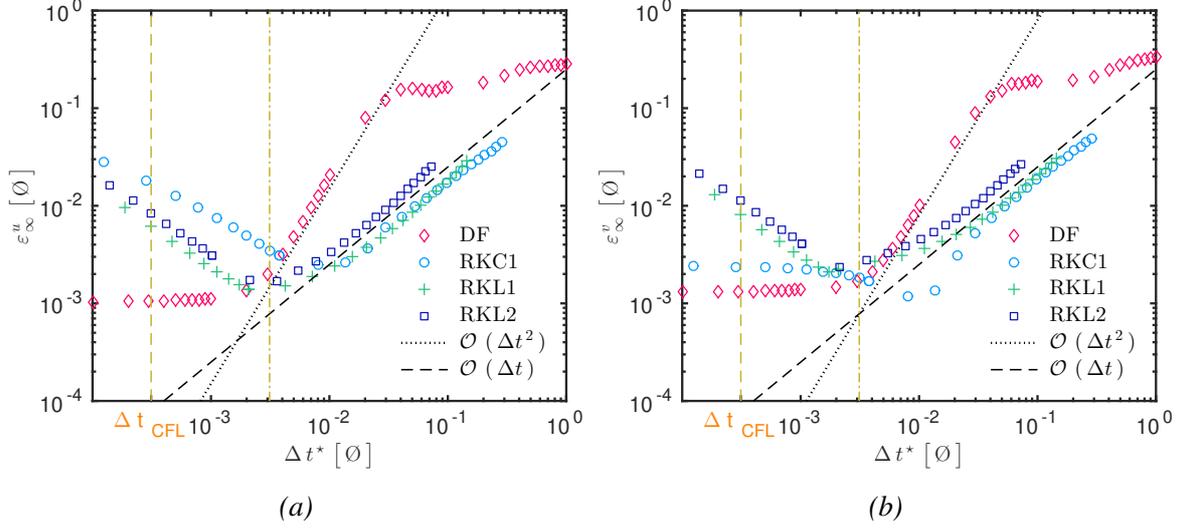In terms of the CPU time, it can be noticed, that among all methods the simulation with the

20

Figure 6: $\mathcal{L}_\infty$ error as a function of $\Delta t^\star$ for dimensionless u (a) and v (b).

Table 1: Comparison of the numerical results for the linear case study. The number of super-time-steps: $N_{\mathrm{S}} = 10$.

	EULER	**DF**	**RKC1**	**RKL1**	**RKL2**
Time-step $\Delta t^\star$	2.81×10^{-4}	10^{-3}	2.81×10^{-2}	1.55×10^{-2}	7.59×10^{-3}
Total number of time-steps	85 333	24 000	853	1 552	3 160
$\varrho_{N_t}\,[\%]$	100	28.13	1.00	1.82	3.70
ε_∞: v	1.31×10^{-3}	1.35×10^{-3}	4.64×10^{-3}	3.97×10^{-3}	4.57×10^{-3}
ε_∞: u	1.04×10^{-3}	1.10×10^{-3}	4.85×10^{-3}	2.83×10^{-3}	3.43×10^{-3}
Digit accuracy: v	3.02	3.03	2.23	2.61	2.71
Digit accuracy: u	3.17	3.13	2.30	2.76	2.58
CPU time $[\mathsf{s}]$	1.64	0.56	0.15	0.37	1.18
$\varrho_{\mathrm{CPU}}\,[\%]$	100	34.15	9.15	22.56	71.95
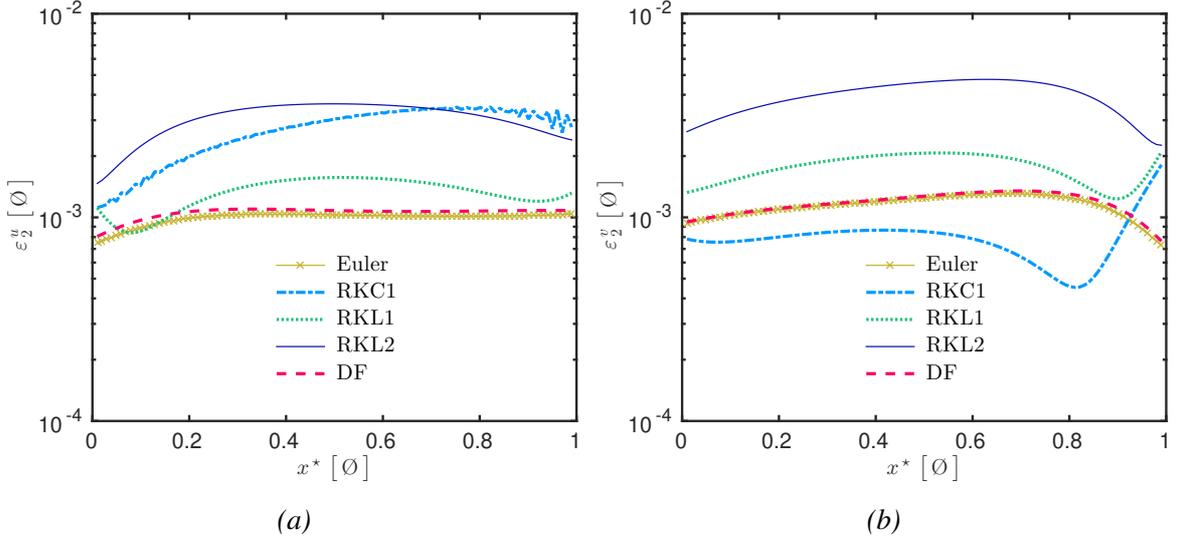
Figure 7: Error between the numerical simulation results and reference solution, for $\Delta t^\star$ values presented in Table 1 and $\Delta x^\star = 10^{-2}$.

RKC1 method takes only 9 % of the CPU time required by the EULER explicit discretization. The notable difference between the STS schemes can be explained with the intermediate RUNGE–KUTTA-like calculations (see the scheme of the method in Figure 3b). From Figure 8, it can be seen how a size of N_S influences the overall efficiency of the simulations (the test was made for N_S up to 150).

The error increases with N_S, because a bigger N_S implies a wider superstep. Hence, fewer discretization points and less accuracy from the simulation are obtained. The ratios ϱ_{CPU} and ϱ_{N_t}, on the other hand, are decreasing functions of N_S. Therefore, depending on the requirement, a bigger N_S can be taken to perform faster simulations but with a higher error. The recommended horizon for the choice of N_S can be bounded with $N_S = 100$, because, after this point, the required CPU time remains almost stable while the error becomes bigger. The convergence paths of $\mathcal{O}\left(N_S^2\right)$ for the errors and ratio ϱ_{N_t} are consistent with the Equations (3.9)–(3.11) to obtain supersteps Δt_S. In terms of the order of convergence of $\mathcal{O}\left(N_S\right)$ for the computational time ratio ϱ_{CPU}, the dependence can be clearly seen from the Figure 3b. As the STS methods perform N_S intermediate steps, the computational time shall increase by the total number of supersteps.

Last but not least, one can also observe that among all three schemes the RKL2 method is the weakest with higher errors and ratios. From Table 1 it can also be seen that the CPU time with the RKL2 method is shorter only for 30% than the explicit scheme. Therefore, for further investigation, it is proposed to omit the implementation of the RKL2 scheme and continue with the RKC1 and RKL1.

4.2 Second case: nonlinear heat and mass transfer model

The linear case was studied to validate methods for a faster simulation and to verify the convergence of schemes. The second case study, which is nonlinear, is more realistic as material properties are in correlation with the surrounding field and taken as functions of the dimensionless moisture content and temperature.
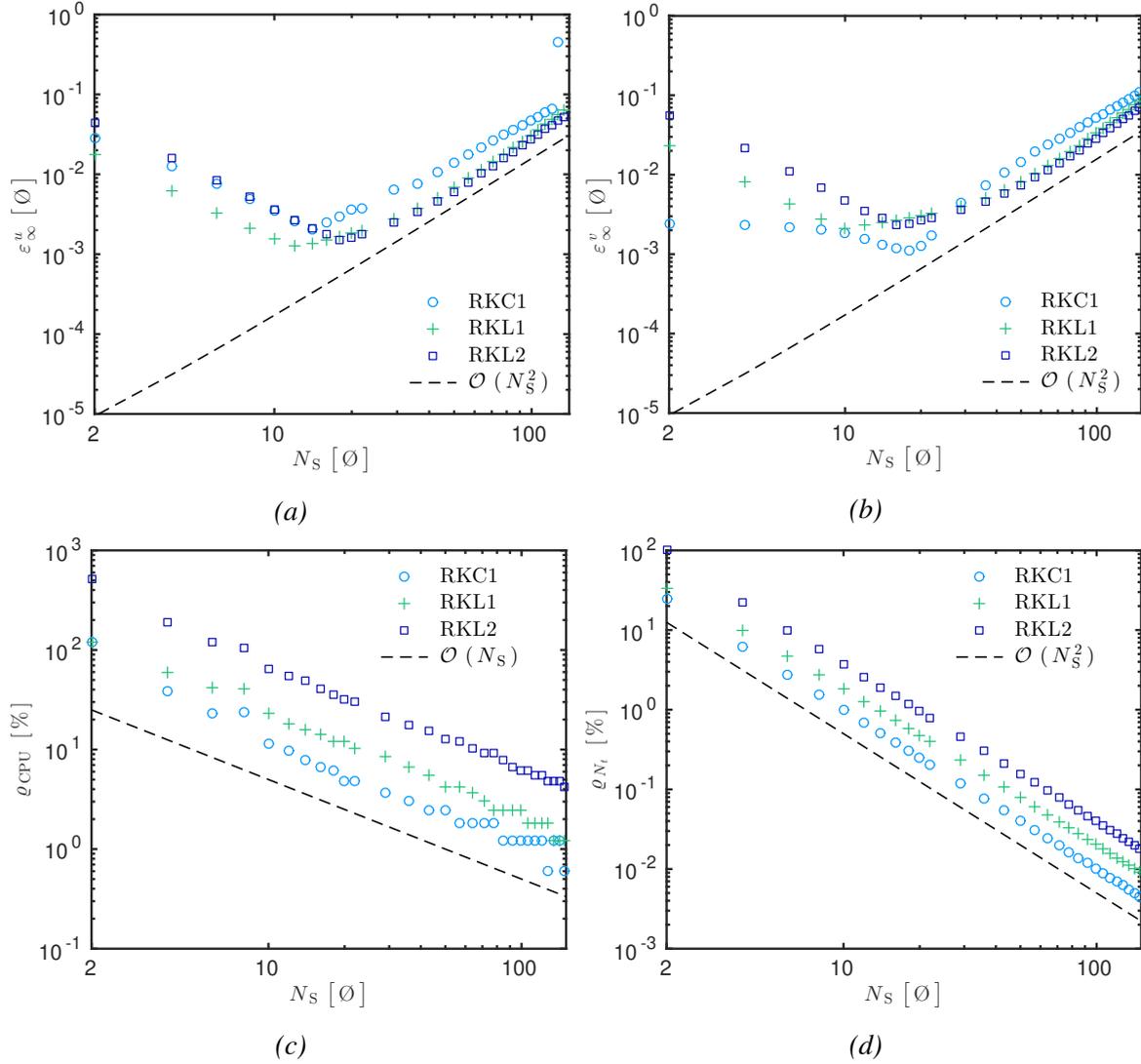
22

Figure 8: Influence of the number of supersteps N_S on $\mathcal{L}_\infty$ error (as a function of N_S, compared with the reference solution) for dimensionless u (a) and v (b); on the ratios ϱ_{CPU} (c) and ϱ_{N_t} (d) compared to the EULER explicit scheme results.
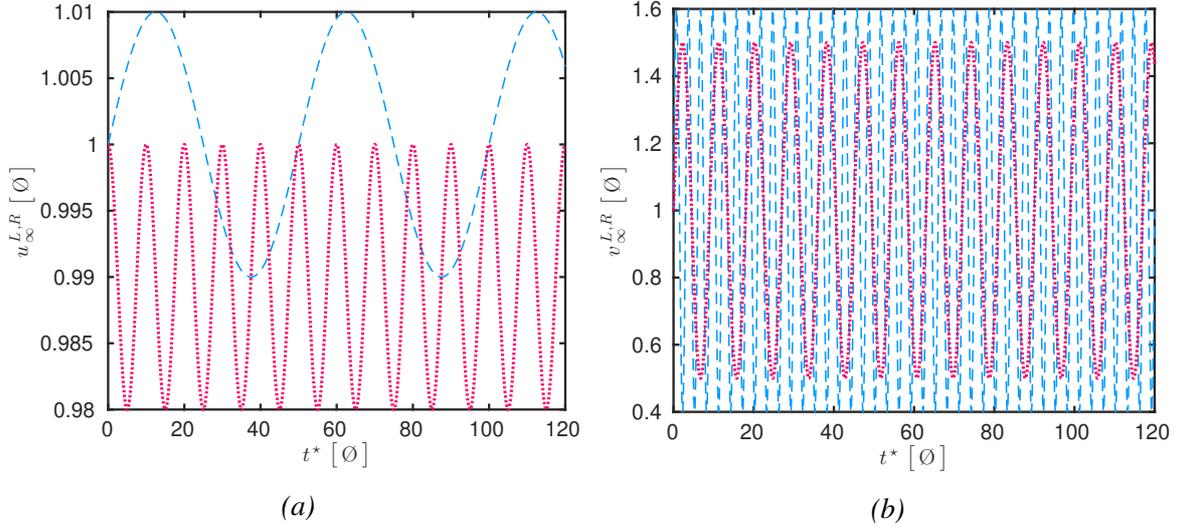
Figure 9: Variations of boundary data, at $x^\star = 0$ in blue *dashed line and at $x^\star = 1$ in* red *dotted line, for dimensionless u (a) and v (b).*

4.2.1 Case study

As the validation for the linear case was successful for the dimensionless form of the model, the same technique is used for the second case too. The variations of the boundary conditions are given as:

$$x^\star = 0: \quad u_\infty^L = 1 + \frac{1}{100} \sin\left(2\pi \frac{t^\star}{50}\right), \qquad v_\infty^L = 1 - \frac{3}{5} \sin\left(2\pi \frac{t^\star}{3}\right),$$

$$x^\star = 1: \quad u_\infty^R = 1 - \frac{1}{50} \sin\left(2\pi \frac{t^\star}{20}\right)^2, \qquad v_\infty^R = 1 + \frac{1}{2} \sin\left(2\pi \frac{t^\star}{9}\right),$$

and are presented in Figure 9.

The initial conditions for u and v are identically equal to one. More details on the description of the case can be found in [27] and in Appendix A.2.

4.2.2 Results and discussion

In this case study only three schemes are compared, namely DU FORT–FRANKEL, RUNGE–KUTTA–CHEBYSHEV and RUNGE–KUTTA–LEGENDRE methods of the first order. For each of these schemes, different discretization parameters of the time domain are applied. For DU FORT–FRANKEL this parameter equals $\Delta t^\star = 10^{-3}$.

The time discretization for the STS schemes should be computed with the Formulas (3.9) and (3.10). The required explicit time-step is chosen according to the Equation (3.17) to be $\Delta t^\star_{\exp} = 2.16 \cdot 10^{-5}$. By applying this result with the number of super-time-steps $N_S = 10$ to the formulas, one can get $\Delta t^\star_{RKC1} = 2.16 \cdot 10^{-3}$ and $\Delta t^\star_{RKL1} = 1.19 \cdot 10^{-3}$ as supersteps for RUNGE–KUTTA–CHEBYSHEV and RUNGE–KUTTA–LEGENDRE methods of the first order respectively. It can be noted that the STS method allows increasing the size of the time domain discretization by increasing the value of supersteps N_S. This might have an impact on the reduction of the CPU time performance compared to the EULER explicit scheme. The efficiency of the methods is further reported on Table 2. The most remarkable point is the number of time-steps used by

24

Table 2: Computational time and accuracy of results of four schemes for nonlinear case study. The number of super-time-steps: $N_S = 10$.

	EULER	DF	RKC1	RKL1
Time-step Δt	2.16×10^{-5}	10^{-3}	2.16×10^{-3}	1.19×10^{-3}
Total number of time-steps	5 567 953	120 000	55 680	101 236
$\varrho_{N_t} [\%]$	100	2.12	1.00	1.81
ε_∞: v	1.94×10^{-4}	2.01×10^{-4}	3.73×10^{-4}	2.96×10^{-4}
ε_∞: u	1.51×10^{-4}	1.50×10^{-4}	1.77×10^{-4}	2.39×10^{-4}
Digit accuracy: v	3.64	3.81	3.83	3.72
Digit accuracy: u	4.05	4.08	3.54	3.74
CPU time [s]	1 298	32	103	200
$\varrho_{CPU} [\%]$	100	2.44	8.00	15.45

each method. It can be noted that the DF and RKL1 methods require only 2% of the total time-steps number of the EULER explicit method, and the RKC1 method computes only 1% of it. The accuracy of digits (SCD) is almost 4 for all schemes and is slightly higher for simulations of dimensionless u. One can also see that the CPU time for DU FORT–FRANKEL simulation is only 2% of time needed for the EULER explicit method, whereas the STS methods take 8% (RKC1) and 15% (RKL1). These results are consistent since $N_S = 10$ and the numerical time-stepping methods RKC1 and RKL1 require intermediate RUNGE–KUTTA-like iterations between two super-time-steps.

The accuracy of the simulations can be observed from the profiles of dimensionless temperature and volumetric moisture content, which are presented in Figures 10 and 11. It can be seen that both STS methods produce results in very good agreement with the reference solution.

Further from Figure 12, which shows the error in comparison with the reference solution, one can see that schemes perform very well for quite stringent error tolerance levels. Table 2 also demonstrates that the global uniform error $\mathcal{L}_\infty$ and the digit accuracy are compatible among studied method. Overall, it can be concluded that while obtaining almost the same level of accuracy, all three methods proved to be much more efficient than the EULER explicit method in terms of the CPU time gain and wider discretization sizes.

5 Comparison with experimental observations

Previous sections aimed at quantifying the accuracy and efficiency of the numerical models. The analysis was made according to the numerical error in reference to the "exact" solution, obtained with the the Matlab open source package Chebfun [48]. This section is aimed to analyze the *fidelity* of the numerical models [16, 17]. One can refer to the fidelity as a quantitative measure to evaluate the ability of the numerical approximations with the governing equations to reproduce the observed data. In this paper, the $\mathcal{L}_\infty$ error given by Eq. (3.18) is applied as a measure of the fidelity. The application to the real case study is the next step to validate the fidelity of the proposed numerical models for long-term simulations. The predictions of the numerical models are now compared with more than 14 months of experimental observations, obtained in previous investigations for drying of a rammed earth wall [28–30].
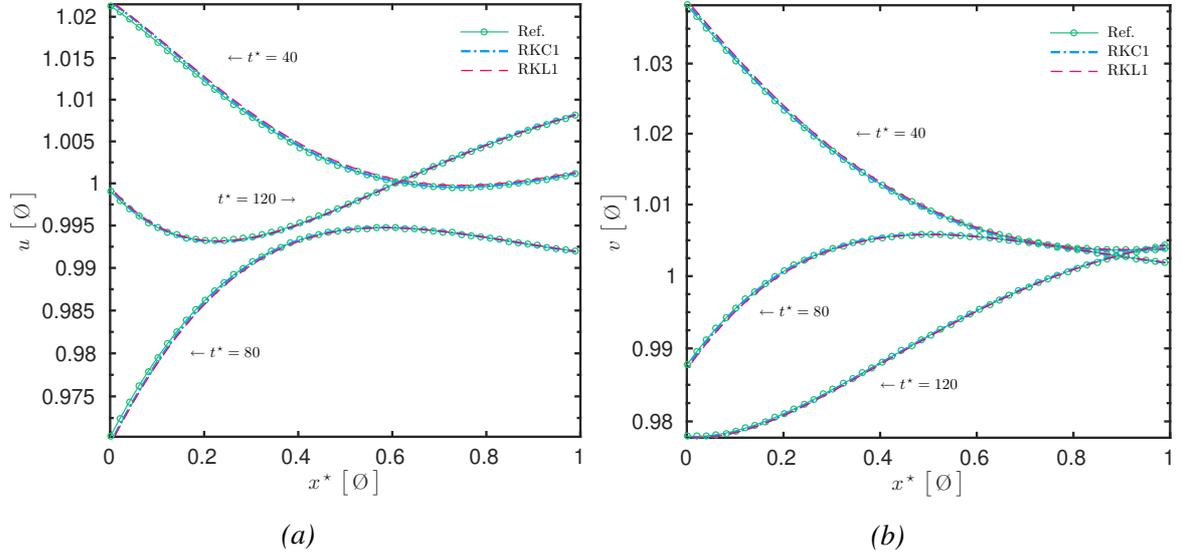
Figure 10: Dimensionless u (a) and v (b) profiles at $t^\star = 40$, $t^\star = 80$ and $t^\star = 120$, for $\Delta t^\star$ values presented in Table 2 and $\Delta x^\star = 10^{-2}$.
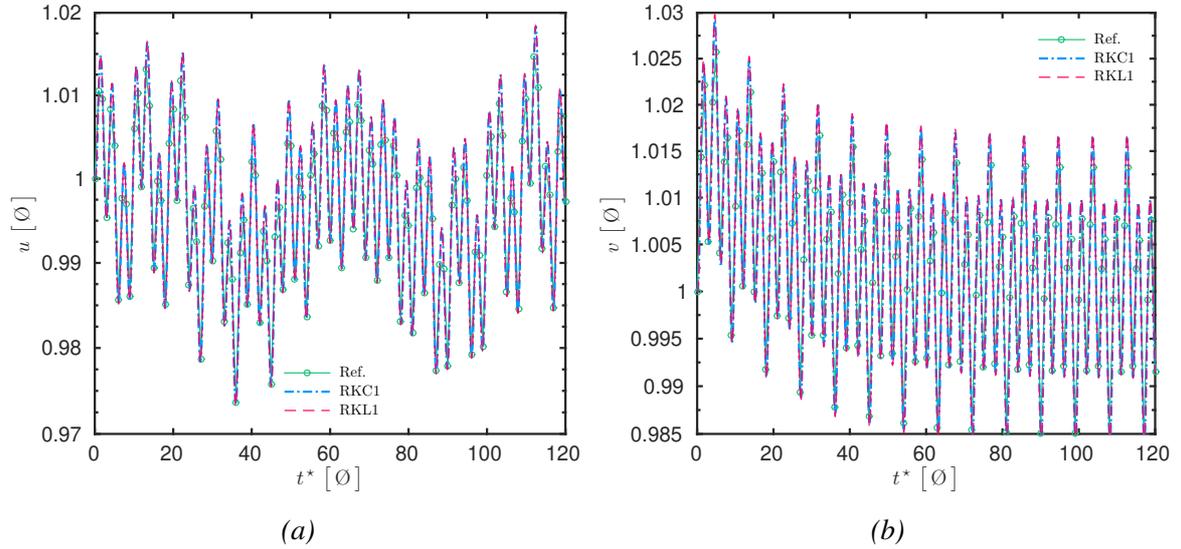
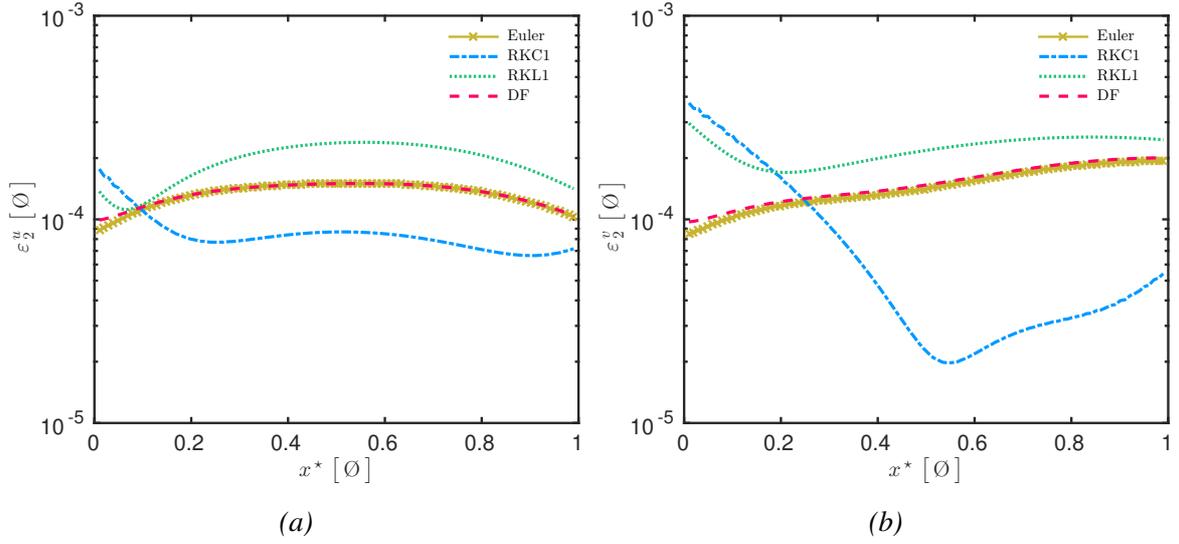*Figure 11: Dimensionless u (a) and v (b) evolutions at $x^\star = 0.5$, for $\Delta t^\star$ values presented in Table 2 and $\Delta x^\star = 10^{-2}$.*

(a) *(b)*

Figure 12: Error between the numerical simulation results and reference solution, for $\Delta t^{\star}$ values presented in Table 2 and $\Delta x^{\star} = 10^{-2}$.

Figure 13: Overview of one of the boxes with an open door (on the left), and the central data-logger with the temperature and relative humidity control group (right) from [28].

5.1 Experimental set up

The experimental setup consists of a $1 \times 1.5 \times 0.3 \ [\mathrm{m}^3]$ sized and initially saturated rammed earth wall. It is placed in a double climatic box. The picture and schematic illustration can be seen in Figures 13, 14 and 15.

Relative humidity and temperature variations are monitored in two boxes. One should notice that the boundary conditions are controlled on one side of the wall, as illustrated in Figure 14. The sensors are placed in the middle of the wall on a central horizontal plane at the height of $0.5 \ [\mathrm{m}]$, on surfaces of the wall and inside boxes. As a result of measurements, the data for approximately 14 months' time period is available. In particular, the following values have been recorded: *(i)* the variations of the ambient humidity and temperature in the boxes; *(ii)* the temperature in the middle and on surfaces of the rammed earth wall; *(iii)* the moisture content in the middle of the rammed earth wall.

Part of the experiment, which imposes additional difficulty is that doors of boxes are occasionally opened during the experiments. These sequences are highlighted in Figure 16a. They lead to changes in heat and mass surface transfer coefficients, particularly by making them varying in time.
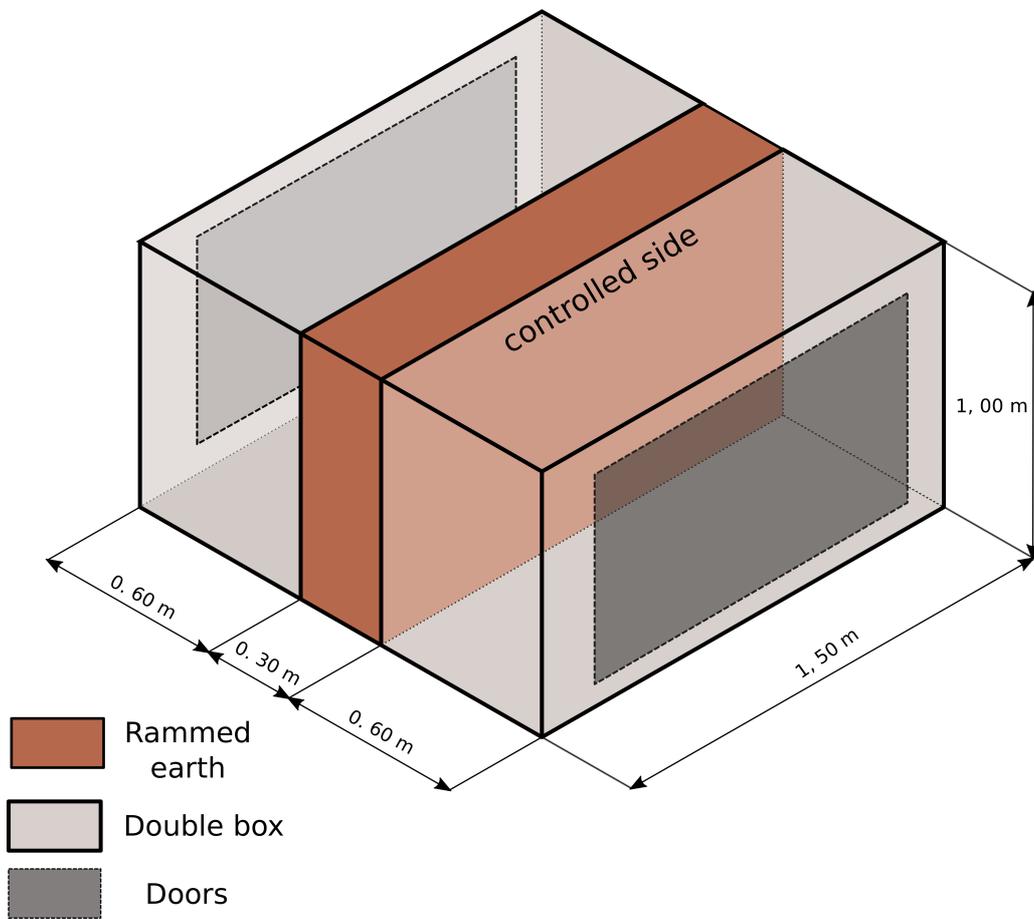
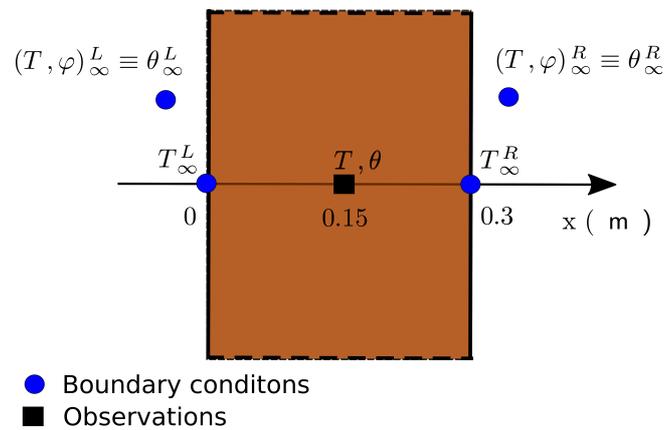Figure 14: *Scheme of the wall, placed in a double climatic box with doors.*

Figure 15: *Illustration of the experimental design with the position of the sensors for the temperature, relative humidity and moisture content.*
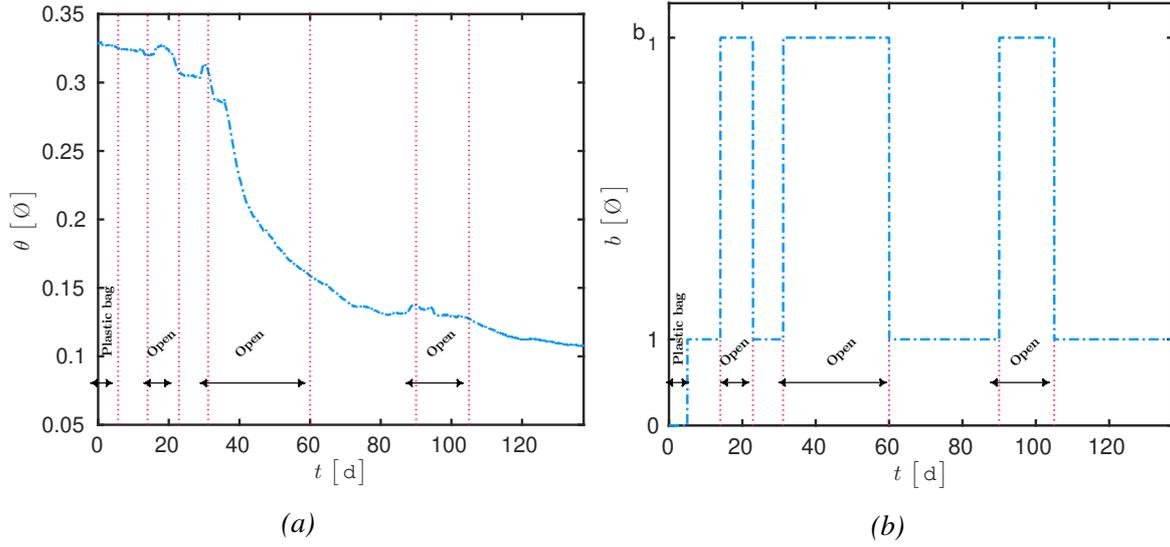
Figure 16: Plot of the mass content and specifically designed function $b(t)$ with sequences of opening and closing doors during the first four months of experiment.

5.2   Parameters for the mathematical model

The heat and moisture transport inside the rammed earth wall is simulated using the system of nonlinear coupled partial differential equations given in Eq. (2.6). The material properties are taken according to Refs. [29, 30, 50]. The specific heat capacity and dry mass are equal to $c_0 = 648 \left[\mathsf{J/(kg \cdot K)} \right]$ and $\rho_0 = 1730 \left[\mathsf{kg/m^3} \right]$ respectively. The diffusion coefficients under temperature and moisture gradient are equal to $D_T = 10^{-11} \left[\mathsf{m^2/(s \cdot K)} \right]$ and $D_\theta(\theta) = 10^{-8} + 2 \cdot 10^{-10} \cdot \theta \left[\mathsf{m^2/s} \right]$. The function of the thermal conductivity k_T as a function of θ is expressed as $k_T(\theta) = 0.6 + 5 \cdot \theta \left[\mathsf{W/(m \cdot K)} \right]$. The value of the vapor transfer coefficient under a moisture gradient is equal to $k_{TM} = 4 \cdot 10^{-18} \left[\mathsf{kg/(m \cdot s)} \right]$. The values of the thermo-physical constants are as follows: $c_2 = 4185.5 \left[\mathsf{J/(m^3 \cdot K)} \right]$, $L_{12}^\circ = 2.5 \cdot 10^6 \left[\mathsf{J/kg} \right]$, $\rho_2 = 10^3 \left[\mathsf{kg/m^3} \right]$, $R_1 = 2 \cdot 10^{-3} \left[\mathsf{J/(kg \cdot K)} \right]$. Function of relative humidity on mass content is defined as a linear function:

$$\widetilde{\varphi}(\theta) = \frac{\rho_2}{2\,\rho_0} \cdot \theta,$$

and residual function is obtained by function fitting:

$$r(\theta) = \left| 1 - \exp\left(-\frac{4\,\rho_2}{5\,\rho_0} \cdot \theta \right) - \frac{\rho_2}{2\,\rho_0} \cdot \theta \right|.$$

The boundary conditions at the interface of the material with the surrounding environment are of two different types. The temperature of the material at surfaces is measured during the experiment, hence it is known and Equation (2.11) is not used. Instead, a DIRICHLET–type of boundary condition is imposed for temperature:

$$T(x = \{0, \ell\}, t) = T_\infty^{L,R}(t),$$

where the thickness of the wall is $L = 0.3\,\mathsf{m}$ and the time variations of the ambient temperature $T_\infty^{L,R}(t)$ are shown in Figure 17b.
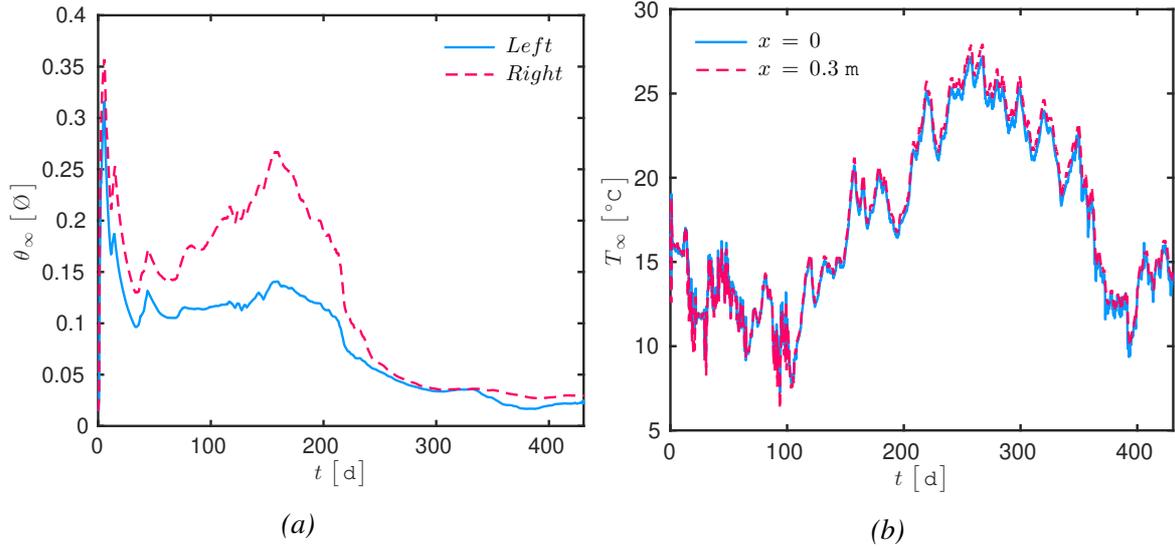
29

Figure 17: Time variations of mass content in the ambient air (a) and of the temperature at surfaces (b).

The mass content at surfaces is not measured directly and the boundary condition is set to be of the ROBIN–type. The Equation (2.10) is slightly modified by introducing the function b depending on time, designed to model the influence of the opening and closing of the box doors:

$$\mathbf{n} \cdot \left(D_\theta \cdot \frac{\partial \theta}{\partial x} + D_T \cdot \frac{\partial T}{\partial x} \right) = b \cdot B \cdot \left(\theta - \theta_\infty(t) \right) - b \cdot G_\infty, \qquad (5.1)$$

where

$$b : t \mapsto b(t), \qquad B : (T, \theta) \mapsto \frac{h_M}{R_1} \cdot \frac{P_{\text{sat}}}{T} \cdot \frac{d\widetilde{\varphi}}{d\theta}, \qquad G_\infty : (T, \theta) \mapsto -\frac{h_M}{R_1} \cdot \frac{P_{\text{sat}}}{T} \cdot r(\theta).$$

The time variations of $\theta_\infty^{L,R}(t)$ in the ambient air are shown in Figure 17a.

The surface convective coefficient is set to $h_M = 10^{-9}\,[\text{m/s}]$. The function $b(t)$ can be seen as a distortion of the latter. According to the state of the box doors, their time variations are shown in Figure 16b. The function $b(t)$ is equal identically to zero for the first 5 days when the wall was built but was placed out of its boxes. During this period, it was sealed with cellophane tape. The range of the function $b(t)$ is equal to 1 and to b_1 when the box doors are closed and opened respectively. The value of the parameter b_1 needs to be estimated since the value of the surface vapor transfer coefficient h_M is not known when the box doors are opened.

As for the initial conditions, the moisture level and temperature within the material are considered to be initially uniform $\theta = 0.33\,[\varnothing]$ and $T = 16.5\,[\,^\circ\text{C}\,]$, respectively.

5.3 Results and discussion

The aim of this section is twofold. The first one is to discuss the reliability of the experimental data, mathematical and numerical models by comparing the numerical predictions to the experimental observations under their uncertainties. The second one is to assess the numerical model fidelity and efficiency.

The discussion of the physical results starts with an evaluation of the uncertainties of experimental measurements. It is one of the important issues that should be considered before starting any comparison with numerical simulations. It can be also mentioned, that these uncertainty
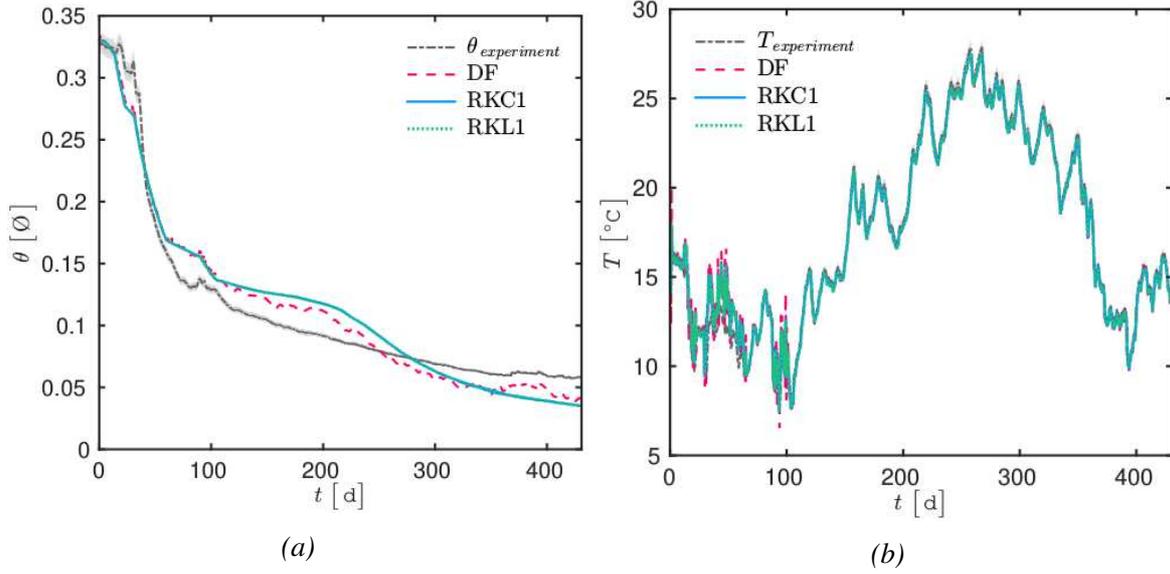
30

Figure 18: Uncertainty of measurements and time evolutions of the mass content (a) and temperature (b) in the middle of the wall in comparison with the three schemes along almost 430 days of the experiment.

measurements were not performed in the works of [28, 29]. Below is the formula to determine uncertainty of measurement:

$$\sigma_m^2 = \sigma_S^2 + \sigma_P^2, \tag{5.2}$$

where σ_S^2 is the sensor accuracy used for the experiments, and σ_P^2 is the positioning sensitivity evaluated numerically.

First of all, the sensor accuracy for mass content and temperature measurement should be identified [51, Chapter 8]. Water content is monitored with the sensors `Campbell CS616`, with the accuracy of $\sigma_S^{\star\theta} = \pm 2.5\,\%$ of volumetric water content and temperature sensors were `Campbell CS215`, the accuracy of which is $\sigma_S^{\star T} = \pm 1.5\,\%$ of temperature in $^\circ C$. The values of accuracy are relative to an absolute standard. So, in order to correctly display the uncertainty of measurement σ_S, the given sensor accuracy values should be multiplied by the measured ones:

$$\sigma_S^\theta = \sigma_S^{\star\theta} \cdot \theta_m, \qquad \sigma_S^T = \sigma_S^{\star T} \cdot T_m, \tag{5.3}$$

where θ_m and T_m are the data obtained from monitoring changes in the middle of the material.

Secondly, positioning accuracy needs to be determined. The accuracy of placement can be taken as $\Delta x_P = 0.5\,\text{cm}$. So, the second term of Equation (5.2) can be evaluated as:

$$\sigma_P^\theta = \frac{\partial\theta}{\partial x} \cdot \Delta x_P, \qquad \sigma_S^T = \frac{\partial T}{\partial x} \cdot \Delta x_P. \tag{5.4}$$

Finally, one can input values obtained from Equations (5.3) and (5.4) to the equality given by Eq. (5.2) to get a corresponding uncertainty of measurement values for water content and temperature with the following equalities:

$$\theta_m^\pm = \theta_m \pm \sigma_m^\theta, \qquad T_m^\pm = T_m \pm \sigma_m^T. \tag{5.5}$$

The uncertainty, determined in this way, is shown in Figure 18.

Next part discusses the fidelity of a mathematical model, *i.e.* the ability of the model to reproduce experimental/physical results. Also, the description of the parameters that were adjusted

31

Table 3: The value of the cost function $\| \theta_{exp.} - \theta_{num} \|$ for each b_1.

	$b_1 = 1$	$b_1 = 4.5$	$b_1 = 6$	$b_1 = 9$
$\| \theta_{exp.} - \theta_{num} \|$ $[\varnothing]$	8.37×10^{-2}	1.48×10^{-2}	1.64×10^{-2}	3.62×10^{-2}

during the implementation is discussed below. The difference between measured data and simulation results can be seen in Figure 18. At first glance, from Figure 18b it can be noticed that the temperature evolution was determined more precisely than the mass content. Discrepancies in simulation results for temperature evolution during the first 100 days of a time period can be explained with the sequences of opening doors. It has to be further studied whether the heat exchange by radiation with other surfaces is significant or not during those openings.

From Figure 18a, it can be seen that simulation results for mass content evolution do not perfectly fit the experimental data. There are several possible explanations for that. First, the material properties, particularly D_θ, are defined by a linear polynomial in θ. The variation of this diffusion coefficient relative to θ may be a different function than the one here assumed. Then, the boundary conditions (5.1) are strongly nonlinear. They have an important influence on the results as it is discussed below. Particularly, the specially designed function $b(t)$, representing the variation of the surface transfer coefficient with the opening/closing of the box doors, has a strong impact on the results. The investigations of its influence are explored below.

Function $b(t)$ is implemented directly in boundary conditions for the mass transfer to model sequences of doors opening (see Figure 16b). However, due to the coupling between two equations of the model given by Eqs. (2.6), it has an impact on both terms. In addition, this function cannot be precisely modelled for at least two reasons: *(i)* the exact number of days when windows were opened is not precisely known from experimental data; *(ii)* air flows in rooms were not measured during those sequences. According to this last point, the surface transfer coefficient has been modelled as a piece-wise constant depending on time. Certainly, the time variations of this coefficient are more complex than this assumption.

Various numerical experiments are performed in order to estimate the impact of function $b(t)$, whose general representation of step-function can be seen from Figure 16b. As one might be mainly concerned with the behavior of simulation results shortly after the end of sequences, the demonstrative tests have been carried out for a 220 days time period. In Figure 19, one can observe the distinct effects of increasing or decreasing the coefficient b_1. Thus, it is adjusted until a better fit is found with $b_1 \approx 4.5$. From the Table 3, it can also be seen that the cost function of $b_1 \approx 4.5$ is the smallest among others. One should note that all these adjustments and computations are possible thanks to fast numerical computations.

Eventually, the importance of flux terms needs to be discussed. The term on the right-hand side of the boundary conditions for the mass content transfer expressed in Eq. (5.1) plays crucial role for model fitting with experimental data as it is discussed below. By neglecting either term, results differ significantly, proving once again the importance of both flux terms. One can first study the case similar to the boundary conditions applied in two previous case studies (linear and nonlinear). Here, the second flux term is neglected:

$$D_\theta \cdot \frac{\partial \theta}{\partial x} + D_T \cdot \frac{\partial T}{\partial x} = b \cdot B \cdot (\theta - \theta_\infty), \qquad (5.6)$$

Figure 20a shows that the drying process with only one flux term is almost twice slower after 40 days. It proves the necessity to include the second term in the boundary flux condition, due to the
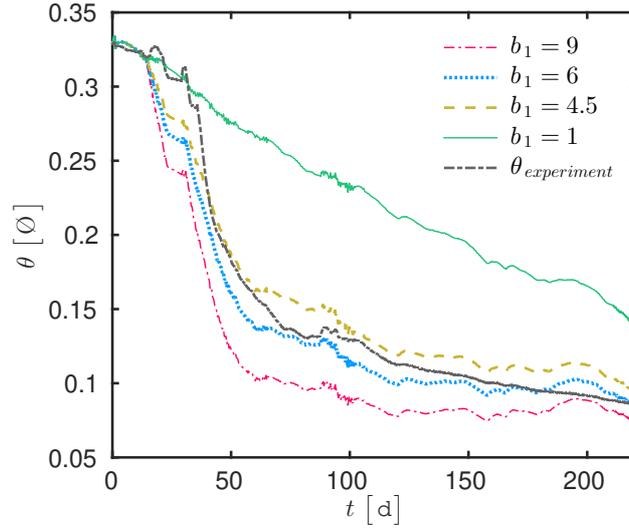
Figure 19: Demonstration of results of tests on parameter b_1 of step-function $b(t)$ illustrated in Figure 16b in comparison with experimental data of the mass content.

temperature and saturation pressure at the surface. The similar pattern of slower drying can be observed in Figure 20 if the first flux term equals to zero:

$$D_\theta \cdot \frac{\partial \theta}{\partial x} + D_T \cdot \frac{\partial T}{\partial x} = -b \cdot G_\infty. \tag{5.7}$$

Conclusively, a good agreement of simulation results with experimental data can be observed by applying full boundary conditions given in Eq. (5.1).

Last point to mention is a relative importance of first and second flux terms in (5.1). One can see the ratio between two time dependent terms in Figure 20b. It can be noticed that both terms are interchangeably important. The term B takes the leading role when difference of moisture content in ambient air increases, as can also be seen in Figure 17a. The term G is important to stabilize periods when drying goes fast and gets steady for a long time at the beginning and at the end of the experiment respectively.

Turning now to the fidelity of numerical results, one can look at the profiles of the relative error in Figure 21. The error remains around $\mathcal{O}(10^{-1})$ for the mass content evolution and for the temperature almost $\mathcal{O}(10^{-2})$ during most of the simulation time. Occasional discrepancies occur because of a few reasons mentioned earlier.

In order to evaluate whether the numerical models over or under predict the experimental data, one can observe Figure 22. As was discussed earlier, due to the difficulty of modelling the function $b(t)$, the simulation results for the mass content evolution both over and underpredict the data conversely (as can be clearly seen from Figure 18a). Interestingly, for the temperature evolution, it is noticeable that the simulation results slightly underestimate the experimental data. Nonetheless, the range of underestimation is within the uncertainty of the sensor as can be seen from Figure 18b. It should be noted, that $f(\sigma_m^\theta)$ is not plotted in Figure 22a because of the very small distribution mean of the uncertainty of measurement of the moisture content $\mathsf{E}(\sigma_m^\theta) = 2 \cdot 10^{-3}\,[\varnothing]$ compared to the distribution mean $\mathsf{E}(\sigma_m^T) = 3 \cdot 10^{-1}\,[°\mathsf{C}]$. To sum up the fidelity measurements, from Table 4, one can observe that the error ε_∞ and the distribution mean E magnitudes show that all three methods perform with the comparable level of accuracy.

More information about the numerical efficiency of the applied methods compared to the EU-LER explicit scheme is provided in Table 5. First of all, it can be seen that the number of required
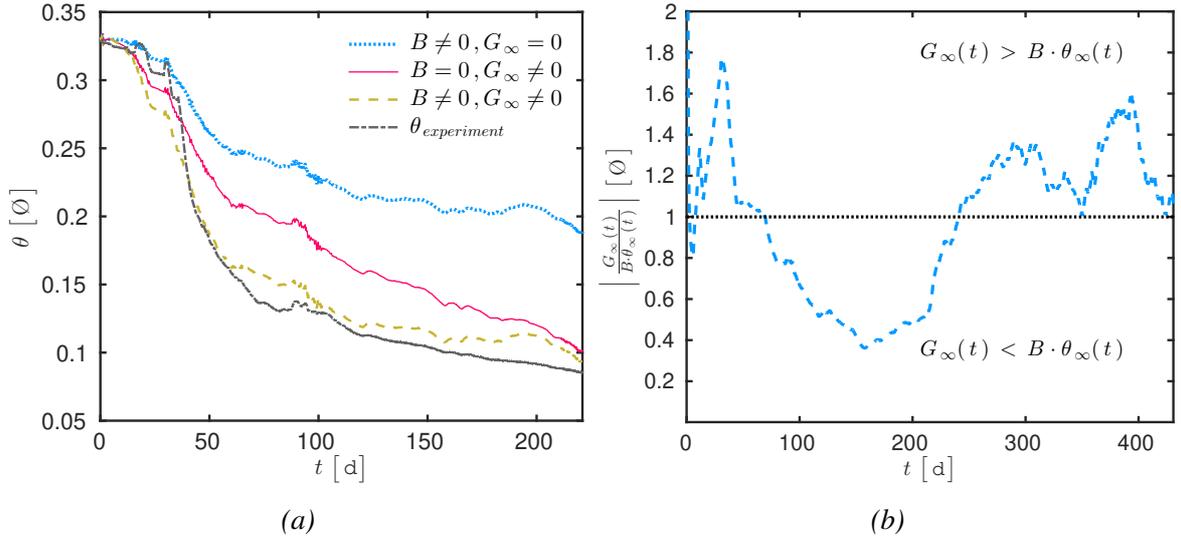
Figure 20: Demonstration of comparative tests for cases when either flux terms of boundary condition given in Eq. (5.1) *equals to zero (a); the ratio between fluxes throughout the time period of experiment (b).*
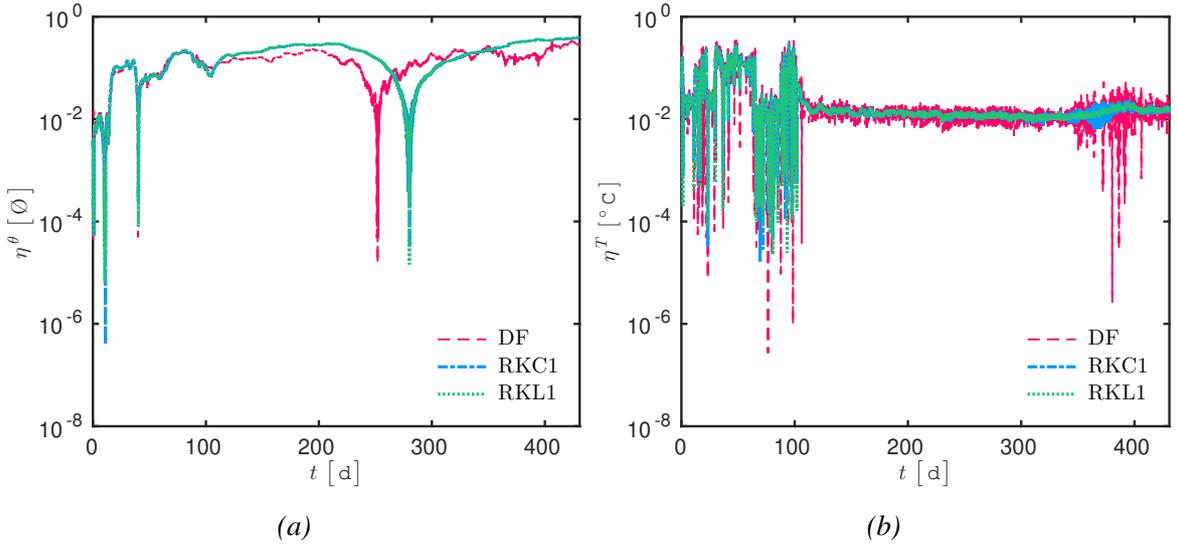

Figure 21: Relative error of the three methods with reference to the experimental data of the mass content (a) and temperature (b).

Table 4: $\mathcal{L}_\infty$ error and E means of the probability density functions of three methods with reference to experimental data.

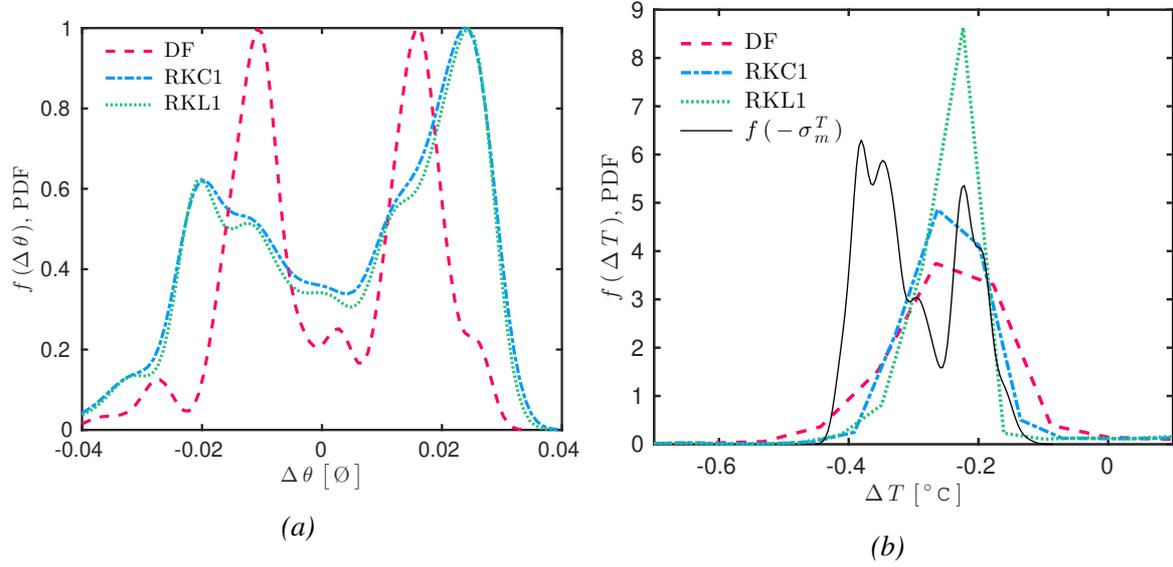|	**DF**	**RKC1**	**RKL1**
ε_∞: Mass content $[\varnothing]$	1.07×10^{-2}	1.91×10^{-2}	1.91×10^{-2}
ε_∞: Temperature $[°\mathsf{C}]$	6.03×10^{-1}	5.53×10^{-1}	5.52×10^{-1}
$\mathsf{E}(\Delta\theta)$: Mass content $[\varnothing]$	1.72×10^{-3}	3.72×10^{-3}	3.71×10^{-3}
$\mathsf{E}(\Delta T)$: Temperature $[°\mathsf{C}]$	-5.45×10^{-2}	-5.41×10^{-2}	-5.39×10^{-2}

34

Figure 22: The distributions of the three methods with reference to the experimental data of the mass content (a) and temperature (b).

Table 5: Comparison of the time-steps and computational times for the experimental case study. The total number of super-time-steps for the STS methods is $N_{\mathrm{S}} = 70$.

	EULER	**DF**	**RKC1**	**RKL1**
Time-step Δt $[\,\mathsf{min}\,]$	1.09×10^{-3}	1×10^{-1}	5.38×10^{-1}	2.73×10^{-1}
Total number of time-steps	9 417 915	103 394	19 220	37 899
$\varrho_{N_t}\,[\,\%\,]$	100	1.1	0.2	0.4
CPU time $[\,\mathsf{h}\,]$	62	1.4	10.7	21.7
$\varrho_{\mathrm{CPU}}\,[\,\%\,]$	100	2.2	17.2	34.8
$\varrho_{\mathrm{CPU}}^{\mathrm{day}}\,[\,\mathsf{s/d}\,]$	520	11	89	181

time-steps is only $1\,\%$ for the DF and $0.2\,\%$, $0.4\,\%$ for the RKC1, RKL1 respectively, comparing to the explicit EULER method. Moreover, in terms of the CPU speed–up, one can observe that all three methods proved to be much faster than the explicit scheme. For the simulation of almost 430 days, the time required for simulations was around 1.4 h, 10 h and 21 h for the DF, RKC1 and RKL1 methods respectively. In addition, the computational time ratio per day of simulation $\varrho_{\mathrm{CPU}}^{\mathrm{day}}$ clearly demonstrates advantages of the proposed numerical models. The DF scheme is leading for the speed of calculation, however, the STS methods were able to perform with the same level of accuracy for larger time-steps. This difference, as was mentioned earlier, is due to the number of intermediate computations between consecutive super-time-step $\Delta\,t_{\mathrm{S}}$ required by the STS approaches. Eventually, all these results prove the computational effectiveness of the numerical schemes to predict long-term heat and mass transfer phenomena through a porous material.

6 Conclusion

Problems of the heat and moisture transfer through porous media of building envelopes are in active discussion since more than half a century. Modern simulation tools have been developed to help manufacturers and builders to better predict the behavior of used materials. Nonetheless, the issue of efficiency of those tools is still persisting. Main concern lies in reducing computational cost and increasing the accuracy of predictions.

In this article, innovative methods, namely the Super–Time–Stepping methods, were proposed to apply on building heat and mass transfer phenomena. It was suggested that those methods can perform accurate simulations with temporal discretization bigger than with standard approaches. Those "super" time-steps are claimed to enable to reduce the computational cost. In addition to that, the design of the methods implies easier application for models in higher dimensions and with nonlinear properties. Moreover, the explicit formulation makes it possible to avoid costly sub-iterations to treat nonlinearities.

The efficiency and reliability of the numerical models have been evaluated for two case studies. A reference solution was taken to evaluate the accuracy of computed solutions. The computational cost of the models was compared to a standard approach such as the EULER explicit method and to an innovative one such as the DU FORT–FRANKEL one. The latter has been recently employed for the simulation of heat and mass transfer in building porous material in Refs. [26, 27]. The first case considered a linear problem. It was used to confirm the theoretical understanding of the numerical methods, particularly for relaxing the stability limits of the scheme. The second case study dealt with a more realistic case by including varying and nonlinear material properties. It was shown, that the numerical models predict the solution with very satisfactory accuracy. The computational efforts were cut by 92% and by 85% for the approach based on CHEBYSHEV and on LEGENDRE orthogonal polynomials respectively.

After these numerical investigations, the fidelity of the proposed models was evaluated for the case of drying of a rammed earth wall. The numerical predictions were compared to experimental observations of moisture content and temperature obtained in previous works [29, 30, 50]. This case requires a long-term simulation since the experimental data is available for more than 14 months. The predictions of the physical model with proposed numerical models show a satisfactory agreement with the experimental observations. As was presented, for a long-term simulation the Super–Time–Stepping methods proved to be much more efficient than the EULER explicit method, which is still widely implemented in building simulation programs. Suggested methods enable to cut the computational cost by more than 5 times.

Another point to mention is that with the STS methods it is possible to make discretization of time domain much longer than it ever was possible before. It should be also noted that the STS methods ensure stability only for super-time-steps. In comparison with the EULER explicit method, where temporal discretization imposed by the CFL stability condition and is of order 10^{-3}, the STS approach enables to implement time-steps at least 100 times longer. This discovery might be crucially beneficial for problems, where temporal evolution flows very fast and a previous fine time domain discretization was costly for such processes.

Moreover, it should be noted that the DU FORT–FRANKEL method is intrusive, while the STS methods are non–intrusive. The DF method is fully discrete, *i.e.* it is a discretization in both space and time domains. Whereas the STS methods can be coupled with any space discretization solvers without any problems, *i.e.* the methods do not depend on an operator. This aspect of the STS methods shall be highly beneficial for any further employment as well.

In general, it can be concluded that the STS methods proved to be both numerically efficient and accurate. The future perspectives are various. Methods can now be tested on broader problems such as two–dimensional simulations of heat and mass transfer.

Acknowledgements

Nomenclature

Parameters involved in the dimensionless representation

δ, γ	coupling parameters	$[\varnothing]$
Bi	BIOT number	$[\varnothing]$
Fo	FOURIER number	$[\varnothing]$
G	additional flux terms	$[\varnothing]$
u, v	fields	$[\varnothing]$

Greek letters

ρ	specific mass	$[\text{kg/m}^3]$
σ_P^2	positioning sensitivity	$[\%]$
σ_S^2	sensor accuracy used for the experiments	$[\%]$
τ	final time	$[\text{h}]$
θ	volumetric moisture (liquid plus vapor) content	$[\varnothing]$

φ	relative humidity	$\big[\,\varnothing\,\big]$

Latin letters

c	heat capacity	$\big[\,\mathsf{J/(kg \cdot K)}\,\big]$
c_T	energy storage coefficient	$\big[\,\mathsf{W \cdot s/(m^3 \cdot K)}\,\big]$
D_θ	diffusion coefficient under moisture gradient	$\big[\,\mathsf{m^2/s}\,\big]$
D_T	diffusion coefficient under temperature gradient	$\big[\,\mathsf{m^2/(s \cdot K)}\,\big]$
h_M	surface vapor transfer coefficient	$\big[\,\mathsf{m/s}\,\big]$
h_T	surface heat transfer coefficient	$\big[\,\mathsf{W/(m^2 \cdot K)}\,\big]$
j_{12}	density of moisture flow rate	$\big[\,\mathsf{kg/(m^2 \cdot s)}\,\big]$
j_q	sensible heat flow rate	$\big[\,\mathsf{W/m^2}\,\big]$
k_T	thermal conductivity of the material	$\big[\,\mathsf{W/(m \cdot K)}\,\big]$
k_{TM}	vapor transfer coefficient under a moisture gradient	$\big[\,\mathsf{kg/(m \cdot s)}\,\big]$
ℓ	thickness of a wall	$\big[\,\mathsf{m}\,\big]$
L_{12}°	latent heat of vaporization	$\big[\,\mathsf{J/kg}\,\big]$
M	molecular mass	$\big[\,\mathsf{kg/mol}\,\big]$
$\mathbf{n}$	outward unit normal vector	$\big[\,\varnothing\,\big]$
P_{sat}	saturation pressure	$\big[\,\mathsf{Pa}\,\big]$
R_1	constant gas for vapor	$\big[\,\mathsf{J/(kg \cdot K)}\,\big]$
t	time	$\big[\,\mathsf{s}\,\big]$
T	temperature	$\big[\,\mathsf{K}\,\big]$
x	thickness coordinate direction	$\big[\,\mathsf{m}\,\big]$

Subscripts

0	dry material
1	water vapor
2	liquid water
∞	ambient air
m	experimental measurement

Superscripts

L, R	left and right boundary values
$\circ$	reference value
$\star$	dimensionless quantity

A Appendix

A.1 Dimensionless parameters for linear case study

For the sake of reproducibility of numerical simulations presented in Section 4.1, we provide here all necessary parameters of the mathematical model.

Material properties expressed with FOURIER numbers, γ and δ which are equal to $\mathrm{Fo}_T = 1.6 \cdot 10^{-1}$, $\mathrm{Fo}_M = 8 \cdot 10^{-2}$, $\gamma = 0$ and $\delta = 2.35 \cdot 10^{-2}$. Other parameters are taken to be equal to 1:

$$D_\theta^\star = D_T^\star = c_T^\star = k_T^\star = k_{TM}^\star = 1.$$

BIOT numbers are expressed as parameters for the boundary conditions and are taken to be equal to:

$$x = 0: \ \mathrm{Bi}_M^{\mathrm{sat},L} = 0, \ \mathrm{Bi}_M^{\theta,L} = 2.55, \ \mathrm{Bi}_T^{T,L} = 5.05, \ \mathrm{Bi}_T^{\mathrm{sat},L} = 0, \ \mathrm{Bi}_T^{\theta,L} = 4.96 \cdot 10^{-1},$$

$$x = 1: \ \mathrm{Bi}_M^{\mathrm{sat},R} = 0, \ \mathrm{Bi}_M^{\theta,R} = 5.18, \ \mathrm{Bi}_T^{T,R} = 1.98, \ \mathrm{Bi}_T^{\mathrm{sat},R} = 0, \ \mathrm{Bi}_T^{\theta,R} = 6.73 \cdot 10^{-2}.$$

Additional flux parameters are taken as $G_M = G_T = 0$. Variation of the boundary data is set to obey te following periodic functions:

$$x = 0: \ u_\infty^L = 1 + \frac{3}{5} \sin\left(2\pi \cdot \frac{t}{5}\right)^2, \qquad v_\infty^L = 1 + \frac{1}{5} \sin\left(2\pi \cdot \frac{t}{2}\right)^2,$$

$$x = 1: \ u_\infty^R = 1 + \frac{1}{2} \sin\left(2\pi \cdot \frac{t}{3}\right)^2, \qquad v_\infty^R = 1 + \frac{9}{10} \sin\left(2\pi \cdot \frac{t}{6}\right)^2.$$

A.2 Dimensionless parameters for nonlinear case study

For the sake of reproducibility of numerical simulations presented in Section 4.2, we provide here all necessary parameters of the mathematical model. The problem is considered with $\mathrm{Fo}_T = 1.61 \cdot 10^{-1}$, $\mathrm{Fo}_M = 1.16 \cdot 10^{-2}$, $\gamma = 2.35 \cdot 10^{-2}$ and $\delta = 1.5 \cdot 10^{-1}$. Dimensionless material properties are defined as follows:

$$D_\theta^\star(v) = 4.045\, v^{6.448} + 16.23,$$

$$D_T^\star(u) = 0.4 + 3.4\, u,$$

$$c_T^\star(v) = \frac{246.6\, v^2 - 778.9\, v + 656.9}{v^4 - 41.37\, v^3 + 395.2\, v^2 - 985.6\, v + 760.7},$$

$$k_T^\star(v) = \frac{15.3\, v^2 - 46.53\, v + 38.04}{v^4 - 10.46\, v^3 + 46.24\, v^2 - 85.34\, v + 56.1},$$

$$k_{TM}^\star(v) = \frac{1.644\, v^2 - 7.013\, v + 7.505}{v^4 - 3.133\, v^3 + 4.859\, v^2 - 8.003\, v + 7.408}.$$

BIOT numbers of the boundary conditions are taken to be equal to:

$$x = 0: \ \mathrm{Bi}_M^{\mathrm{sat},L} = 0, \ \mathrm{Bi}_M^{\theta,L} = 3.65, \ \mathrm{Bi}_T^{T,L} = 6.45, \ \mathrm{Bi}_T^{\mathrm{sat},L} = 0, \ \mathrm{Bi}_T^{\theta,L} = 0.514,$$

$$x = 1: \ \mathrm{Bi}_M^{\mathrm{sat},R} = 0, \ \mathrm{Bi}_M^{\theta,R} = 5.48 \cdot 10^{-1}, \ \mathrm{Bi}_T^{T,R} = 2.06, \ \mathrm{Bi}_T^{\mathrm{sat},R} = 0, \ \mathrm{Bi}_T^{\theta,R} = 7.72 \cdot 10^{-2}.$$

Additional flux parameters are taken as $G_M = G_T = 0$.

References

[1] M. Woloszyn and C. Rode. Tools for performance simulation of heat, air and moisture conditions of whole buildings. In *Building Simulation*, volume 1, pages 5–24. Springer, 2008.

[2] A. S. Guimarães, J. Delgado, A. C. Azevedo, and V. P. de Freitas. Interface influence on moisture transport in buildings. *Construction and Building Materials*, 162:480–488, 2018.

[3] B.C. Bauklimatik Dresden. *Simulation Program for the Calculation of Coupled Heat, Moisture, Air, Pollutant, and Salt Transport.* 2011.

[4] I.B.P. Fraunhofer. *Wufi.* 2005.

[5] N. Mendes, M. Chhay, J. Berger, and D. Dutykh. *Numerical methods for diffusion phenomena in building physics: A practical introduction*. PUCPRess, 2017.

[6] A. Luikov. *Heat and mass transfer in capillary bodies*. New York, NY: Pergamon Press, 1966.

[7] W. J. Ferguson and I. W. Turner. A comparison of the finite element and control volume numerical solution techniques applied to timber drying problems below the boiling point. *International Journal for Numerical Methods in Engineering*, 38(3):451–467, 1995.

[8] H. Thomas, K. Morgan, and R. Lewis. A fully nonlinear analysis of heat and mass transfer problems in porous bodies. *International Journal for Numerical Methods in Engineering*, 15(9):1381–1393, 1980.

[9] F. Tariku, K. Kumaran, and P. Fazio. Transient model for coupled heat, air and moisture transfer through multilayered porous media. *International journal of heat and mass transfer*, 53(15):3035–3044, 2010.

[10] J. Langmans, A. Nicolai, R. Klein, and S. Roels. A quasi-steady state implementation of air convection in a transient heat and moisture building component model. *Building and Environment*, 58:208–218, 2012.

[11] C. Belleudy, M. Woloszyn, M. Chhay, and M. Cosnier. A 2d model for coupled heat, air, and moisture transfer through porous media in contact with air channels. *International Journal of Heat and Mass Transfer*, 95:453–465, 2016.

[12] K. Abahri, R. Bennacer, and R. Belarbi. Sensitivity analyses of convective and diffusive driving potentials on combined heat air and mass transfer in hygroscopic materials. *Numerical Heat Transfer, Part A: Applications*, 69(10):1079–1091, 2016.

[13] M. Simo-Tagne, R. Rémond, Y. Rogaume, A. Zoulalian, and B. Bonoma. Modeling of coupled heat and mass transfer during drying of tropical woods. *International Journal of Thermal Sciences*, 109:299 – 308, 2016.

[14] A. Paepcke and A. Nicolai. Performance analysis of coupled quasi-steady state air flow calculation and dynamic simulation of hygrothermal transport inside porous materials. *Energy Procedia*, 132:759–764, 2017.

[15] T. Hong, J. Langevin, and K. Sun. Building simulation: Ten challenges. In *Building Simulation*, pages 1–28. Springer, 2018.

[16] M. P. Clark and D. Kavetski. Ancient numerical daemons of conceptual hydrological modeling: 1. fidelity and efficiency of time stepping schemes. *Water Resources Research*, 46(10), 2010.

[17] D. Kavetski and M. P. Clark. Ancient numerical daemons of conceptual hydrological modeling: 2. impact of time stepping schemes on model analysis and prediction. *Water Resources Research*, 46(10), 2010.

[18] W. Gentzsch. Numerical solution of linear and non-linear parabolic differential equations by a time-discretisation of third order accuracy. *Proceedings of the third GAMM—Conference on Numerical Methods in Fluid Mechanics*, pages 109–117, 1980.

[19] K. Gurski and S. O'Sullivan. A stability study of a new explicit numerical scheme for a system of differential equations with a large skew-symmetric component. *SIAM Journal on Numerical Analysis*, 49(1):368–386, 2011.

[20] C. D. Meyer, D. S. Balsara, and T. D. Aslam. A second-order accurate super timestepping formulation for anisotropic thermal conduction. *Monthly Notices of the Royal Astronomical Society*, 422(3):2102–2115, 2012.

[21] C. D. Meyer, D. S. Balsara, and T. D. Aslam. A stabilized Runge–Kutta–Legendre method for explicit super-time-stepping of parabolic and mixed equations. *Journal of Computational Physics*, 257:594–626, 2014.

[22] P. Schrooyen, A. Turchi, K. Hillewaert, P. Chatelain, and T. E. Magin. Two-way coupled simulations of stagnation-point ablation with transient material response. *International Journal of Thermal Sciences*, 134:639 – 652, 2018.

[23] J.-J. Droux. Three-dimensional numerical simulation of solidification by an improved explicit scheme. *Computer Methods in Applied Mechanics and Engineering*, 85(1):57–74, 1991.

[24] V. Alexiades. Overcoming the stability restriction of explicit schemes via super-time-stepping. *Proceedings of Dynamic Systems and Applications*, 2:39–44, 1995.

[25] V. Alexiades, G. Amiez, and P.-A. Gremaud. Super-time-stepping acceleration of explicit schemes for parabolic problems. *Communications in numerical methods in engineering*, 12(1):31–42, 1996.

[26] S. Gasparin, J. Berger, D. Dutykh, and N. Mendes. Stable explicit schemes for simulation of nonlinear moisture transfer in porous materials. *Journal of Building Performance Simulation*, 11(2):129–144, 2018.

[27] S. Gasparin, J. Berger, D. Dutykh, and N. Mendes. An improved explicit scheme for whole-building hygrothermal simulation. In *Building Simulation*, volume 11, pages 465–481. Springer, 2018.

[28] P.-A. Chabriac. *Mesure du comportement hygrothermique du pisé*. PhD thesis, ENTPE; CNRS-LTDS (UMR 5513), 2014.

[29] L. Soudani, A. Fabbri, J.-C. Morel, M. Woloszyn, P.-A. Chabriac, H. Wong, and A.-C. Grillet. Assessment of the validity of some common assumptions in hygrothermal modeling of earth based materials. *Energy and Buildings*, 116:498–511, 2016.

[30] L. Soudani, M. Woloszyn, A. Fabbri, J.-C. Morel, and A.-C. Grillet. Energy evaluation of rammed earth walls using long term in-situ measurements. *Solar Energy*, 141:70–80, 2017.

[31] J. R. Philip and D. A. De Vries. Moisture movement in porous materials under temperature gradients. *Eos, Transactions American Geophysical Union*, 38(2):222–232, 1957.

[32] N. Mendes, P. C. Philippi, and R. Lamberts. A new mathematical method to solve highly coupled equations of heat and mass transfer in porous media. *International Journal of Heat and Mass Transfer*, 45(3):509–518, 2002.

[33] G. H. dos Santos, N. Mendes, and P. C. Philippi. A building corner model for hygrothermal performance and mould growth risk analyses. *International Journal of Heat and Mass Transfer*, 52(21-22):4862–4872, 2009.

[34] H. M. Künzel. Simultaneous heat and moisture transport in building components. *One-and two-dimensional calculation using simple parameters. IRB-Verlag Stuttgart*, 1995.

[35] H. Auracher. *Wasserdampfdiffusion und Reifbildung in porösen Stoffen: Mitteilung aus dem Institut für Technische Thermodynamik und Thermische Verfahrenstechnik der Universität Stuttgart*. VDI-Verlag, 1974.

[36] S. Gasparin, J. Berger, D. Dutykh, and N. Mendes. An adaptive simulation of nonlinear heat and moisture transfer as a boundary value problem. *International Journal of Thermal Sciences*, 133:120–139, 2018.

[37] O. Coussy. *Poromechanics*. John Wiley & Sons Ltd., 2004.

[38] D. J. Struik. *A source book in mathematics, 1200-1800*, volume 11. Harvard University Press, 1969.

[39] J. Berger, S. Gasparin, D. Dutykh, and N. Mendes. Accuracy of numerical methods applied to building energy performance. 2017.

[40] A. Trabelsi, Z. Slimani, and J. Virgone. Response surface analysis of the dimensionless heat and mass transfer parameters of medium density fiberboard. *International Journal of Heat and Mass Transfer*, 127:623–630, 2018.

[41] A. H. Nayfeh. *Perturbation methods*. John Wiley & Sons, 2008.

[42] S.V. Patankar. Numerical fluid flow and heat transfer. *Hemisphere, New York*, 1980.

[43] E. C. Du Fort and S. P. Frankel. Stability conditions in the numerical treatment of parabolic differential equations. *Mathematical Tables and Other Aids to Computation*, 7(43):135–152, 1953.

[44] R. D. Richtmyer and K. W. Morton. Difference methods for initial-value problems. *Interscience, New York*, 1967.

[45] P. J. Taylor. The stability of the Du Fort-Frankel method for the diffusion equation with boundary conditions involving space derivatives. *The Computer Journal*, 13(1):92–97, 1970.

[46] R. Courant, K. Friedrichs, and H. Lewy. On the partial difference equations of mathematical physics. *IBM journal of Research and Development*, 11(2):215–234, 1967.

[47] V Markov. On functions least deviated from zero on a given interval. *St. Petersburg (in Russian). German translation: Uber Polynome, die in einem gegeben Intervalle möglichst wenig fon Null abweichen. Math. Ann*, 77(1916):213–258, 1892.

[48] T. A. Driscoll, N. Hale, and L. N. Trefethen. *Chebfun guide*. Pafnuty Publications, Oxford, 2014.

[49] G. Söderlind and L. Wang. Evaluating numerical ODE/DAE methods, algorithms and software. *Journal of computational and applied mathematics*, 185(2):244–260, 2006.

[50] L. Soudani, A. Fabbri, M. Woloszyn, P.-A. Chabriac, A.-C. Grillet, and J.-C. Morel. Etude de la pertinence des hypothèses dans la modélisation hygrothermique du pisé. In *Proceedings of French Speaking Conference of the International Building Performance*, 2014.

[51] L. Soudani. *Modelling and experimental validation of the hygrothermal performances of earth as a building material*. PhD thesis, Lyon, 2016.